Delft University of Technology

Faculty of EEMCS

Loop-to-Loop Pulsed Electromagnetic Field Signal Transfer in Layered Configurations - Application to Inter-Chip Wireless Communication

MSc. Thesis

Author:
Vincent Voogt
Student number:
1505327

Supervisors:
Dr. Ir. I. E. Lager
Dr. Ir. B. J. Kooij

MSc. Programme:
Electrical Engineering

Specialisation:
Telecommunications

June 28, 2013

Contents

Preface **i**

1 Introduction **1**

1.1 Background 1

1.2 Outline of this thesis 1

1.3 Notational conventions 2

2 Configuration **5**

2.1 Actual IC fabrication process 5

2.2 The examined configuration 6

2.3 Antennas 7

3 Radiated field **9**

3.1 Time domain 9

3.2 Transform domain 10

4 Dispersive behaviour of the reflection coefficient at the conducting interface **13**

5 Determining the space-time expression of the magnetic Hertzian vector potential **17**

5.1 Application of the inverse Fourier transform 17

5.2 Obtaining the general space-time expression 18

5.3 Difference between the instantaneous and dispersive response 21

6 Determining the space-time expression of the electric and magnetic field components **23**

6.1 Application of the Cagniard-deHoop method for the electric field 24

6.2 Application of the Cagniard-deHoop method for the magnetic field 25

7 Numerical implementation **29**

7.1 Determination of the arrival time as a function of q 29

7.2 Determination of the upper boundary of the integral with respect to q as a function of τ 31

7.3 Determination of the values on the Cagniard-deHoop contour 32

7.4 Coordinate stretching of the integrals 33

7.4.1 Stretching of the initial part of the Green's function 33

7.4.2 Stretching of the dispersive part of the Green's function 33

8 Numerical results **35**

8.1 The source signature 35

8.2 Validation against established results 36

8.2.1 A magnetic dipole in free-space 37

8.2.2 Reflection with a conducting layer 38

8.3 Investigation of a realistic configuration 39

9 Conclusion and future work **47**

A Pole contribution at τ **49**

A.1 First order pole 49

A.2 Second order pole 50

Preface

This work has been performed as a MSc. graduation project at Delft University of Technology on the topic 'Loop-to-loop pulsed electromagnetic field signal transfer in layered configurations - application to inter-chip wireless communication'. The goal of this project was the derivation of an analytic expression for the space-time Green's function in the case of a loop-to-loop pulsed signal transfer in a layered configuration. The study has important implications in the chip-to-chip digital signal transfer.

This work will be assessed by:

- Prof. Dr. Ir. A. Neto *(supervising professor)*
- Dr. Ir. I. E. Lager *(supervisor)*
- Dr. Ir. B. J. Kooij *(supervisor)*
- Dr. Ir. M. D. Verweij

Name: Vincent Voogt
Date: June 24$^{\text{th}}$ 2013

Chapter 1

Introduction

1.1 Background

In 1965 Gordon E. Moore wrote a paper with observations and a predictive statement concerning the increase in number of components in integrated circuits (IC's) by a factor of two every two years [14, 13]. This statement has later become known as "Moore's Law" and has proven to be an accurate 'rule of thumb' for over half a century [12].

Recent studies however show the appearance of some major fundamental bottlenecks [1, 3, 11, 17]. Unlike the downscaling of transistors, which in general provide improvements in performance through the reduction of the intrinsic gate delay, interconnects end up in decreasing overall performance due to longer delays and parasitic effects.

Even though solutions are found that counteract the negative effect of interconnects on the overall chip performance, they often need more exotic materials or special fabrication processes which considerably increase production costs. Furthermore, these solutions often only postpone the moment of reaching the fundamental limits of wired interconnects [3].

Other studies have investigated the use of wireless interconnects for inter- and intra chip communication using wireless (pulsed-field) signal transfer [2, 8, 15, 25]. This solution provides a low-cost and low-power alternative to conventional wire interconnects while still enabling high data-rate communication at short range.

1.2 Outline of this thesis

While pulsed-field, wireless interconnects offer clear advantages, a lot of research still needs to be conducted before the technology is sufficiently mature for its introduction in (mass-production) electronics. Recent works have has been focused on the generating and handling of the (coded) pulses [16] and the implementation of specific applications, such as on-chip antennas for clock distribution [8, 15, 25]. However, most results concerning actual signal transfer are limited to experimental measurements.

In [10], initial work has been done regarding the development of an actual analytic time-domain model for the loop-to-loop pulsed-field for wireless interconnects. There, the generated voltage at the receiving antenna is characterized for different types of *causal pulses* using the electromagnetic field/source reciprocity theorem of the convolution type. However, the configuration discussed in this study is not representative for an integrated circuit (IC), since the coupling path was taken as free-space.

This thesis will therefore serve as the logical next step in the investigation of wireless interconnects,

by examining a configuration that is representative of IC antenna structures. Given the layered nature of IC design, the modified Cagniard method (or 'Cagniard-DeHoop') will provide the proper tool to obtain closed-form time domain expressions for the electromagnetic (EM) field components. A preliminary study along these lines have been recently published in [21].

The starting point of the thesis is an analysis made in Chapter 2 of the fabrication process of a loop antenna embedded in an IC. This analysis is subsequently employed for constructing a *model configuration* that is amenable to an analytic study, this study being the core contribution of this work. To this end, a Hertzian vector potential based formulation is developed in Chapter 3. The relevant space-time dependent state variables will be subject to a succession of Laplace and Fourier transforms, the applicable equations being thus handled in the spectral domain. In Chapter 4 the dispersive behavior due to the conductivity will be discussed. The obtained results will then be transformed back to space-time by using the Cagniard-De Hoop method in Chapter 5, thus providing a closed form analytical solution for the Hertzian vector potential in space-time. Chapter 6 will then discuss the additional steps necessary to derive the actual values for the electric and magnetic field components. The method uses to implement the obtained analytical solution in a numerical program is discussed in Chapter 7. Numerical results for known solutions, as well as a typical configuration are given in Chapter 8. Conclusions concerning the present work and considerations for future work are given in Chapter 9.

1.3 Notational conventions

Any position $\boldsymbol{x}$ in the $\mathbb{R}^3$ is specified by the coordinates $\{x_1, x_2, x_3\}$ with respect to a right-handed orthogonal Cartesian reference frame. Using the three mutually perpendicular base unit-vectors $\boldsymbol{i}_m$ ($m \in 1, 2, 3$), each position can then be described by a position vector

$$\boldsymbol{x} = x_1\boldsymbol{i}_1 + x_2\boldsymbol{i}_2 + x_3\boldsymbol{i}_3. \tag{1.1}$$

The time coordinate is t.

The position of the transmit antenna will be denoted by $\boldsymbol{x}^T \in \mathbb{R}^3$, whereas the position of the receive antenna will be denoted by $\boldsymbol{x}$. The *relative* position with regard to the transmit antenna is denoted via the vector $\boldsymbol{X} = \boldsymbol{x} - \boldsymbol{x}^T$.

Alternatively, a position can also be specified in a cylindrical reference frame $\{r, \phi, x_3\}$ by

$$x_1 = r\cos(\phi) \tag{1.2}$$

$$x_2 = r\sin(\phi) \tag{1.3}$$

$$x_3 = x_3 \tag{1.4}$$

with $r = \left[x_1^2 + x_2^2\right]^{\frac{1}{2}}$, $0 \leqslant \phi < 2\pi$ and x_3.

Partial differentiation with regard to position coordinates x_m ($m \in 1, 2, 3$) will be denoted by ∂_m, while partial differentiation with regard to time will be denoted by ∂_t.

In this thesis work, all quantities are subjected to a Laplace transform with respect to time t and a Fourier transform with respect to the position coordinates x_1 and x_2.

The Laplace transformation of an arbitrary function $f(\boldsymbol{x}, t)$ is

$$\hat{f}(\boldsymbol{x}, s) = \mathcal{L}\left\{f(\boldsymbol{x}, t)\right\} = \int_{t=0}^{\infty} f(\boldsymbol{x}, t)\exp[-st]\mathrm{d}t, \quad \text{for } s \in \mathbb{R},\ s > 0 \tag{1.5}$$

with s representing the Laplace transform variable. This choice of the s parameter ensures that the integral in the right hand side of (1.5) is convergent as long as the function $f(\boldsymbol{x}, t)$ is bounded. The

latter requirement is always met since $f(\boldsymbol{x},t)$ depends on physical quantities, which themselves have always bounded values.

Furthermore, by choosing s real and positive this set corresponds to a Lerch's sequence, this yielding a unique one-to-one mapping of (1.5) by virtue of Lerch's theorem [24].

The Fourier transform of an arbitrary function $\hat{f}(\boldsymbol{x},s)$ in Laplace transform domain is

$$\begin{aligned}\tilde{f}(\alpha_1,\alpha_2,x_3,s) &= \mathcal{F}\left\{\hat{f}(\boldsymbol{x},s)\right\}\\ &= \int_{x_1=-\infty}^{\infty}\int_{x_1=-\infty}^{\infty}\hat{f}(x_1,x_2,x_3,s)\exp[s(\alpha_1x_1+\alpha_2x_2)]\mathrm{d}x_1\mathrm{d}x_2, \quad \text{for } \alpha_1,\alpha_2\in\mathbb{C}\end{aligned} \tag{1.6}$$

where $s\alpha_1$ and $s\alpha_2$ represent the transform parameters. Here s is included for the later application of the Cagniard-deHoop method. The parameters α_1 and α_2 are taken to be purely imaginary, i.e., $\{\alpha_{1,2}\in\mathbb{C};\mathrm{Re}\{\alpha_{1,2}\}=0\}$.

Finally, the inverse Fourier transform of an arbitrary function $\tilde{f}(\alpha_1,\alpha_2,x_3,s)$ is given by

$$\begin{aligned}\hat{f}(\boldsymbol{x},s) &= \mathcal{F}^{-1}\left\{\tilde{f}(\alpha_1,\alpha_2,x_3,s)\right\}\\ &= \left(\frac{s}{2\pi\mathrm{i}}\right)^2\int_{\alpha_2=-\mathrm{i}\infty}^{\mathrm{i}\infty}\int_{\alpha_1=-\mathrm{i}\infty}^{\mathrm{i}\infty}\tilde{f}(\alpha_1,\alpha_2,x_3,s)\exp[-s(\alpha_1x_1+\alpha_2x_2)]\mathrm{d}\alpha_1\mathrm{d}\alpha_2.\end{aligned} \tag{1.7}$$

Chapter 2

Configuration

This chapter will give an introduction to the configuration discussed in this thesis. A simplified, but illustrative, model will be derived from the fabrication process of an actual Integrated Circuit (IC).

This simplified model will allow for the determination of the electric field strength $\boldsymbol{E}$ (Vm^{-1}) and the magnetic field strength $\boldsymbol{H}$ (Am^{-1}) outside the IC via the Cagniard-DeHoop method.

2.1 Actual IC fabrication process

During the fabrication process of a general IC one usually starts with a pure silicon ($\varepsilon_r \sim 11.7$, $\mu_r \sim 1$, $\sigma \sim 10^{-3}$ Sm^{-1}) wafer with a thickness of about 1 mm, as a basis. On top of this wafer several processing steps are applied in order to create the desired IC. These processing steps can be roughly divided in two categories, namely FEOL (front end of line) and BEOL (back end of line) processing.

FEOL processing steps are all steps that are undertaken to create the transistors, which are embedded directly into the silicon. The various steps during this part of the fabrication process remove, add, pattern and change the various materials and their electric properties.

BEOL processing steps are all steps that focus on connecting the various transistors such that the actual circuits are formed by creating metal interconnects in various layers. These interconnects are isolated by insulation material which can be, for example, silicon dioxide (SO_2; $\varepsilon_r \sim 3.9$, $\mu_r \sim 1$, $\sigma \sim 10^{-18}$ Sm^{-1} [1]).

It is clear that after the FEOL and BEOL processing steps a highly heterogeneous and, possibly, anisotropic medium results. When considering the fabrication process of an integrated antenna, this is often fabricated on the top of the metal layers in which the interconnects are fabricated (during the BEOL process) often followed by a dielectric passivation layer. This passivation layer can consist of a thick resin, which has a similar relative permittivity as the silicon dioxide.

However, when designing IC's with components whose performance can be influenced by the presence of interconnects and transistors (such as antennas, but also inductors) it is quite common to keep the region around these components 'clean' within a certain guard area. This means that within this area there are no interconnects and transistors. Therefore the presence of interconnects and transistors can be neglected when considering an electromagnetic model for an integrated antenna.

[1] http://www.siliconfareast.com/sio2si3n4.htm

Table 2.1: Electromagnetic properties of the configuration under investigation

Domain	Relative permittivity ε_r	Relative permeability μ_r	Conductivity σ (Sm^{-1})
$\mathcal{D}_1$	1	1	0
$\mathcal{D}_2$	3.9	1	0
$\mathcal{D}_3$	11.7	1	10^{-3}

2.2 The examined configuration

A model configuration is now assembled based on the fabrication process described in the previous section. This model consists essentially of 3 planar layers, of which the top and bottom are assumed to be semi-infinite half-spaces. A schematic of the configurations is shown in Fig.2.1.

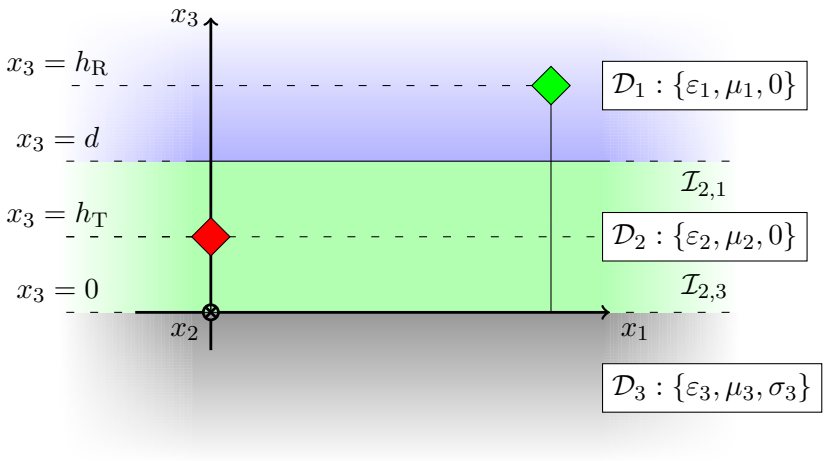

Figure 2.1: Schematic of the Configuration

A pure silicon layer $\mathcal{D}_3 = \{-\infty < x_1 < \infty, -\infty < x_2 < \infty, x_3 < 0\}$ with $\sigma_3 >> 0$, $\varepsilon_3 > \varepsilon_0$ and $\mu_3 = \mu_0$ is chosen as the basis of the IC-model. Due to conductive losses the silicon layer can be modeled as a infinite half-space.

On top of the conductive silicon layer a thin dielectric slab (in the order of a few micrometers) $\mathcal{D}_2 = \{-\infty < x_1 < \infty, \ -\infty < x_2 < \infty, 0 < x_3 < d\}$ is placed in which the transmit antenna is embedded. This layer represents the so called 'metal layers' as well as the passivation layers. The conductivity of the silicon dioxide is deemed to be more than sufficiently small to be approximated as zero. It is assumed that the passivation layer has indeed a matched permittivity and therefore these two layers are not distinguished from each other from an electromagnetic point of view.

Finally, the top layer $\mathcal{D}_1 = \{-\infty < x_1 < \infty, -\infty < x_2 < \infty, x_3 > d\}$ is taken to be free space. Furthermore, since $\mathcal{D}_1$ is modeled as a infinite half-space there exist only waves propagating away from $\mathcal{D}_2$ in $\mathcal{D}_1$. The receive antenna is located in $\mathcal{D}_1$.

In summary, the table 2.1 shows the chosen electromagnetic properties of the configuration under investigation.

2.3 Antennas

As mentioned in Section 2.2 the transmit and receive antennas are located in $\mathcal{D}_2$ and $\mathcal{D}_1$ respectively. Both antennas are taken to be loop with vanishingly small wire diameter and vectorial areas $\boldsymbol{A}^{\{T,R\}} = A^{\{T,R\}}\boldsymbol{i}_3$, where the superscript T for the transmit antenna and R is used for the receiving antenna. Both antennas are taken to be electrically small.

The position of the transmit antenna is defined by the position of its reference center $\boldsymbol{x}^T$. Since the transmit antenna is located in $\mathcal{D}_2$ the transmit antenna height defined by $x_3 = h_\mathrm{T}$ is taken to be $0 < h_\mathrm{T} < d$. Since the transmit antenna electrically small, it can be modeled as a point source located at its reference center. Furthermore, due to the shift invariance of the configuration in the x_1 and x_2 directions the position of the transmit antenna along these axis can without loss of generality be taken to be $\{x_1, x_2\} = \{0, 0\}$. As a result, the position $\boldsymbol{x}^T$ can be fully described by $\boldsymbol{x}^T = h_\mathrm{T}\boldsymbol{i}_3$.

The position of the receive antenna is defined by the position of its reference center $\boldsymbol{x}$. A superscript R is omitted here since $\boldsymbol{x}$ will always be the point of observation in this thesis. Since the receive antenna is located in $\mathcal{D}_1$ the receive antenna height defined by $x_3 = h_\mathrm{R}$ is taken to be $h_\mathrm{R} > d$. The other position coordinates are taken as $\{x_1, x_2\} \in \mathbb{R}$.

Chapter 3

Radiated field

In this chapter a transform domain expression for the field in $\mathcal{D}_1$ will be derived via the so-called Hertzian vector potential.

3.1 Time domain

Since the transmitting antenna is taken to be electrically small it can be replaced by an equivalent vertical magnetic dipole. If follows from [18] that the radiated EM field can be fully described by the use of a magnetic Hertzian vector potential $\boldsymbol{\Pi}_m(\boldsymbol{X},t)$ as

$$\boldsymbol{E}(\boldsymbol{X},t) = -\mu\boldsymbol{\nabla}\times\partial_t\boldsymbol{\Pi}_m(\boldsymbol{X},t) \tag{3.1}$$

$$\boldsymbol{H}(\boldsymbol{X},t) = \boldsymbol{\nabla}\left(\boldsymbol{\nabla}\cdot\boldsymbol{\Pi}_m(\boldsymbol{X},t)\right) - \mu\varepsilon\partial_t^2\boldsymbol{\Pi}_m(\boldsymbol{X},t) - \mu\sigma\partial_t\boldsymbol{\Pi}_m(\boldsymbol{X},t) \tag{3.2}$$

where $\boldsymbol{E}$, $\boldsymbol{H}$ and $\boldsymbol{\Pi}_m$ depend on the relative position $\boldsymbol{X}$ (see Sec. 1.3) and time t. For compactness of the notation, the dependency on $\boldsymbol{X}$ and t will be omitted in the remainder of this thesis.

The vertical magnetic dipole has the additional property that only the x_3 component is non-zero. As a result, the magnetic Hertz potential $\boldsymbol{\Pi}_m$ can be defined within each layer as

$$\boldsymbol{\Pi}_m = \begin{cases} u^{\mathrm{T};2,1}\boldsymbol{i}_3 & \text{for} \quad \infty < x_3 < d \\ (u^{\mathrm{inc}} + u^{\mathrm{R};2,1} + u^{\mathrm{R};2,3})\boldsymbol{i}_3 & \text{for} \quad d < x_3 < 0 \\ u^{\mathrm{T};2,3}\boldsymbol{i}_3 & \text{for} \quad 0 < x_3 < -\infty \end{cases} \tag{3.3}$$

where the function $u = u(\boldsymbol{X},t)$ represents the different components of $\boldsymbol{\Pi}_m$. The distinction between these components is expressed using different superscripts (as shown in Fig. 3.1), as follows: inc denotes the incident waves (i.e., those that are directly generated by the source), other superscripts reflect either reflection (R) or transmission (T). These superscripts are supplemented by numbers that correspond to the names of the relevant interfaces. The incident field can be found to be [18]

$$u^{\mathrm{inc}}(\boldsymbol{X},t) = \frac{f(t-|\boldsymbol{X}|/c_2)}{4\pi|X|} \tag{3.4}$$

where f represents the magnetic moment of the transmitting loop and

$$c_L = [\varepsilon_L\mu_L]^{\frac{1}{2}}, \quad L = 1,2,3 \tag{3.5}$$

denotes the wave speed in each domain $\mathcal{D}^L$.

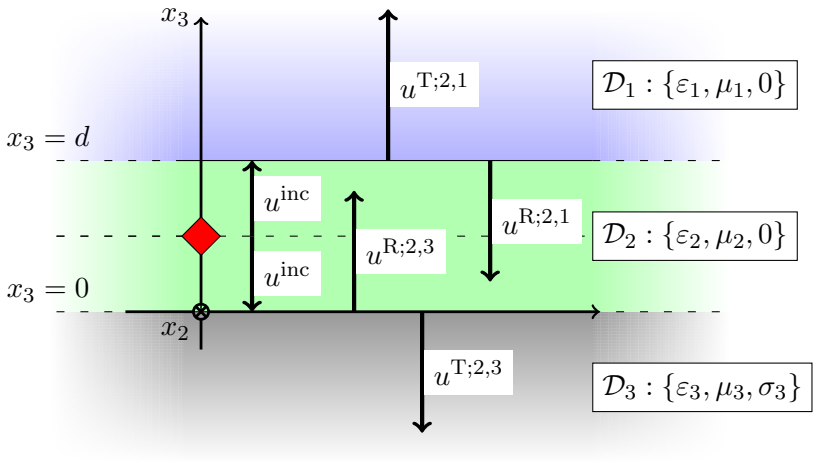

Figure 3.1: Illustrative for the existing u functions in each domain

The remaining functions u satisfy the following wave equations

$$\boldsymbol{\nabla}^2 u^{\mathrm{T};2,1} - c_1^{-2}\partial_t^2 u^{\mathrm{T};2,1} = 0 \tag{3.6}$$

$$\boldsymbol{\nabla}^2 u^{\mathrm{R};2,1} - c_2^{-2}\partial_t^2 u^{\mathrm{R};2,1} = 0 \tag{3.7}$$

$$\boldsymbol{\nabla}^2 u^{\mathrm{R};2,3} - c_2^{-2}\partial_t^2 u^{\mathrm{R};2,3} = 0 \tag{3.8}$$

$$\boldsymbol{\nabla}^2 u^{\mathrm{T};2,3} - c_3^{-2}\partial_t^2 u^{\mathrm{T};2,3} - \sigma_3\mu_3\partial_t u^{\mathrm{T};2,3} = 0. \tag{3.9}$$

These equations are then solved using the boundary conditions

$$\lim_{x_3\downarrow 0}(\partial_3 u^{\mathrm{inc}} + \partial_3 u^{\mathrm{R};2,1} + \partial_3 u^{\mathrm{R};2,3}) = \lim_{x_3\uparrow 0}\partial_3 u^{\mathrm{T};2,3} \tag{3.10}$$

$$\lim_{x_3\downarrow 0}(u^{\mathrm{inc}} + u^{\mathrm{R};2,1} + u^{\mathrm{R};2,3}) = \lim_{x_3\uparrow 0} u^{\mathrm{T};2,3} \tag{3.11}$$

$$\lim_{x_3\uparrow d}(\partial_3 u^{\mathrm{inc}} + \partial_3 u^{\mathrm{R};2,1} + \partial_3 u^{\mathrm{R};2,3}) = \lim_{x_3\downarrow d}\partial_3 u^{\mathrm{T};2,1} \tag{3.12}$$

$$\lim_{x_3\uparrow d}(u^{\mathrm{inc}} + u^{\mathrm{R};2,1} + u^{\mathrm{R};2,3}) = \lim_{x_3\downarrow d} u^{\mathrm{T};2,1}. \tag{3.13}$$

3.2 Transform domain

Equations (3.4), (3.6)-(3.13) are now subject to a Laplace transform with resprect to time (see (1.5)) and a Fourier transform in space (see (1.6)). As a result of these transformation it follows that $\partial_t \to s$ and $\partial_{1,2} \to -s\alpha_{1,2}$ and, therefore, $\partial_{1,2}^2 \to s^2\alpha_{1,2}^2$.

The transform representation for the incident wave is then

$$\tilde{u}^{\mathrm{inc}}(\alpha_1, \alpha_2, x_3, s) = \frac{\hat{f}(s)}{2s\gamma_2}\exp[-s\gamma_2\,|x_3 - h_{\mathrm{T}}|] \tag{3.14}$$

as also given in [7]. Furthermore, after applying the transformations, (3.6)-(3.9) become

$$\partial_3^2\tilde{u}^{\mathrm{T};2,1} - s^2\gamma_1^2\tilde{u}^{\mathrm{T};2,1} = 0 \tag{3.15}$$

$$\partial_3^2\tilde{u}^{\mathrm{R};2,1} - s^2\gamma_2^2\tilde{u}^{\mathrm{R};2,1} = 0 \tag{3.16}$$

$$\partial_3^2\tilde{u}^{\mathrm{R};2,3} - s^2\gamma_2^2\tilde{u}^{\mathrm{R};2,3} = 0 \tag{3.17}$$

$$\partial_3^2\tilde{u}^{\mathrm{T};2,3} - s^2\left[\gamma_3^2 + s^{-1}\sigma_3\mu_3\right]^{\frac{1}{2}}\tilde{u}^{\mathrm{T};2,3} = 0 \tag{3.18}$$

where

$$\gamma_{1,2,3} = \left[c_{1,2,3}^{-2} - (\alpha_1^2 + \alpha_2^2)\right]^{\frac{1}{2}} \tag{3.19}$$

represents the propagation coefficient. To ensure a one-to-one mapping between γ_L and its square root the condition is imposed that $\mathrm{Re}\{\gamma_L\} \geqslant 0$. For the same reason, a second condition is imposed on (3.18) such that $\mathrm{Re}\{\gamma_3^2 + s^{-1}\sigma_3\mu_3\} \geqslant 0$.

The second order differential equations (3.15)-(3.18) can be solved for their respective functions $\tilde{u}$. Their solutions, which remain bounded as $|x_3| \to \infty$, are given by

$$\tilde{u}^{\mathrm{R};2,1} = A^{\mathrm{R};2,1} \exp[s\gamma_2(x_3 - d)] \tag{3.20}$$

$$\tilde{u}^{\mathrm{R};2,3} = A^{\mathrm{R};2,3} \exp[-s\gamma_2 x_3] \tag{3.21}$$

$$\tilde{u}^{\mathrm{T};2,1} = A^{\mathrm{T};2,1} \exp[-s\gamma_1(x_3 - d)] \tag{3.22}$$

$$\tilde{u}^{\mathrm{T};2,3} = A^{\mathrm{T};2,3} \exp[s\left[\gamma_3^2 + s^{-1}\sigma_3\mu_3\right]^{\frac{1}{2}} x_3] \tag{3.23}$$

where the functions $A^{\mathrm{R};2,1}$, $A^{\mathrm{R};2,3}$, $A^{\mathrm{T};2,1}$ and $A^{\mathrm{T};2,3}$ follow from the application of the boundary conditions. These conditions are given in the transform domain by

$$\lim_{x_3\downarrow 0}(\partial_3\tilde{u}^{\mathrm{inc}} + \partial_3\tilde{u}^{\mathrm{R};2,1} + \partial_3\tilde{u}^{\mathrm{R};2,3}) = \lim_{x_3\uparrow 0}\partial_3\tilde{u}^{\mathrm{T};2,3} \tag{3.24}$$

$$\lim_{x_3\downarrow 0}(\tilde{u}^{\mathrm{inc}} + \tilde{u}^{\mathrm{R};2,1} + \tilde{u}^{\mathrm{R};2,3}) = \lim_{x_3\uparrow 0}\tilde{u}^{\mathrm{T};2,3} \tag{3.25}$$

$$\lim_{x_3\uparrow d}(\partial_3\tilde{u}^{\mathrm{inc}} + \partial_3\tilde{u}^{\mathrm{R};2,1} + \partial_3\tilde{u}^{\mathrm{R};2,3}) = \lim_{x_3\downarrow d}\partial_3\tilde{u}^{\mathrm{T};2,1} \tag{3.26}$$

$$\lim_{x_3\uparrow d}(\tilde{u}^{\mathrm{inc}} + \tilde{u}^{\mathrm{R};2,1} + \tilde{u}^{\mathrm{R};2,3}) = \lim_{x_3\downarrow d}\tilde{u}^{\mathrm{T};2,1}. \tag{3.27}$$

Application of the boundary conditions (3.24)-(3.27) to (3.20)-(3.23) yields

$$\begin{aligned} A^{\mathrm{R};2,1}(s) = &\frac{\hat{f}(s)}{2s\gamma_2}\Big\{\exp[-s\gamma_2(d - h_{\mathrm{T}})] + \hat{R}_{2,3}(s)\exp[-s\gamma_2(d + h_{\mathrm{T}})]\Big\} \\ &\times R_{2,1}\sum_{n=0}^{\infty}\hat{R}_{2,3}^n(s)R_{2,1}^n\exp[-2ns\gamma_2 d] \end{aligned} \tag{3.28}$$

$$\begin{aligned} A^{\mathrm{R};2,3}(s) = &\frac{\hat{f}(s)}{2s\gamma_2}\Big\{\exp[-s\gamma_2 h_{\mathrm{T}}] + R_{2,1}\exp[-s\gamma_2(2d - h_{\mathrm{T}})]\Big\} \\ &\times \hat{R}_{2,3}(s)\sum_{n=0}^{\infty}\hat{R}_{2,3}^n(s)R_{2,1}^n\exp[-2ns\gamma_2 d] \end{aligned} \tag{3.29}$$

$$\begin{aligned} A^{\mathrm{T};2,1}(s) = &\frac{\hat{f}(s)}{2s\gamma_2}\Big\{\exp[-s\gamma_2(d - h_{\mathrm{T}})] + \hat{R}_{2,3}(s)\exp[-s\gamma_2(d + h_{\mathrm{T}})]\Big\} \\ &\times [1 + R_{2,1}]\sum_{n=0}^{\infty}\hat{R}_{2,3}^n(s)R_{2,1}^n\exp[-2ns\gamma_2 d] \end{aligned} \tag{3.30}$$

$$\begin{aligned} A^{\mathrm{T};2,3}(s) = &\frac{\hat{f}(s)}{2s\gamma_2}\Big\{\exp[-s\gamma_2 h_{\mathrm{T}}] + R_{2,1}\exp[-s\gamma_2(2d - h_{\mathrm{T}})]\Big\} \\ &\times \Big[1 + \hat{R}_{2,3}(s)\Big]\sum_{n=0}^{\infty}\hat{R}_{2,3}^n(s)R_{2,1}^n\exp[-2ns\gamma_2 d] \end{aligned} \tag{3.31}$$

where $R_{2,1}$ and $\hat{R}_{2,3}$ represent the reflection coefficients at $\mathcal{I}_{2,1}$ and $\mathcal{I}_{2,3}$, respectively, and are given by

$$R_{2,1} = \frac{\gamma_2 - \gamma_1}{\gamma_2 + \gamma_1} \tag{3.32}$$

$$\hat{R}_{2,3}(s) = \frac{\gamma_2 - \left[\gamma_3^2 + s^{-1}\sigma_3\mu_3\right]^{\frac{1}{2}}}{\gamma_2 + \left[\gamma_3^2 + s^{-1}\sigma_3\mu_3\right]^{\frac{1}{2}}}. \tag{3.33}$$

Furthermore, $[1 + R_{2,1}]$ and $[1 + \hat{R}_{2,3}(s)]$ represent the transmission coefficients at $\mathcal{I}_{2,1}$ and $\mathcal{I}_{2,3}$, respectively.

An inspection of the configuration directly allows verifying the correctness of the u functions, given by the expressions for their respective A functions (see (3.28)-(3.31)). Since the receive antenna will be located in $\mathcal{D}_1$, the main interest in this thesis will be to determine $\tilde{u}^{\mathrm{T};2,1}$. To this end, it is important to identify the various waves contributing at the observation point. These are

- The sum of all waves at $\mathcal{I}_{2,1}$
  - the sum of the waves at $\mathcal{I}_{2,1}$ after generation by the source; their contribution in $\tilde{u}^{\mathrm{T};2,1}$ is given by
    $$\frac{\hat{f}(s)}{2s\gamma_2} \exp[-s\gamma_2(d - h_{\mathrm{T}})]$$
    for the waves that propagate upward after generation by the source, and
    $$\frac{\hat{f}(s)}{2s\gamma_2} \hat{R}_{2,3}(s) \exp[-s\gamma_2(d + h_{\mathrm{T}})]$$
    for the waves that propagate downward after generation by the source and propagate toward $\mathcal{I}_{2,1}$ after reflection at $\mathcal{I}_{2,3}$;
  - the sum of all waves at the interface $\mathcal{I}_{2,1}$ after n reflections at $\mathcal{I}_{2,1}$ and $\mathcal{I}_{2,3}$; this contribution is given by
    $$\sum_{n=0}^{\infty} \hat{R}_{2,3}^n(s) R_{2,1}^n \exp[-2ns\gamma_2 d].$$
- The part of this sum of waves that is actually transmitted into $\mathcal{D}_1$, as given by
  $$[1 + R_{2,1}] \exp[-s\gamma_1(x_3 - d)].$$

Chapter 4

Dispersive behaviour of the reflection coefficient at the conducting interface

In this chapter the reflection coefficient $\hat{R}_{2,3}(s)$ will be discussed in more details. Please note that $\hat{R}_{2,3}(s)$ depends on the Laplace transform parameter s via the non-zero conductivity-related term (3.32), which accounts for the dispersive behavior at $\mathcal{I}_{2,3}$. However, in view of the later application of the Cagniard-DeHoop method, it is not desirable to have a dependence on the s parameter anywhere but in the exponent.

A method which was introduced in [23] will now be applied in order to prepare $\hat{R}_{2,3}(s)$ for its use in the Cagniard-DeHoop method. It is based on determining the inverse Laplace transform of $\hat{R}_{2,3}$, such that in the Cagniard-DeHoop the reflection coefficient can be expressed as the direct Laplace transform of inverse Laplace transformed counterpart. Note that, in order to preclude confusions with the (general) time-domain variable t, the notation κ is used to denote the time dependence for this direct and inverse Laplace transform.

The inverse Laplace transform will be determined using contour integration along a finite branch cut via a method as described in [5, Sec. 26.5]. In order to identify the branch points associated with this branch cut, the reflection coefficient is rewritten as

$$\hat{R}^n_{2,3}(s) = \left[\frac{s\gamma_2 - \gamma_3 s^{\frac{1}{2}}\,(s+\beta)^{\frac{1}{2}}}{s\gamma_2 + \gamma_3 s^{\frac{1}{2}}\,(s+\beta)^{\frac{1}{2}}}\right]^n \tag{4.1}$$

where $\beta = \gamma_3^{-2}\sigma_3\mu_3$ (see (3.30) for details). From (4.1) it is clear that the branch points are $s = 0$ and $s = -\beta$.

The square-roots at the branch points are taken as $\mathrm{Re}\{s^{\frac{1}{2}}\} \geqslant 0$ and $\mathrm{Re}\{(s+\beta)^{\frac{1}{2}}\} \geqslant 0$, in order to ensure a one-to-one mapping. This implies the presence of branch cuts in $\{s \in \mathbb{C}; -\infty < \mathrm{Re}\{s\} < 0; \mathrm{Im}\{s\} = 0\}$ and $\{s \in \mathbb{C}; -\infty < \mathrm{Re}\{s\} < -\beta; \mathrm{Im}\{s\} = 0\}$. Since the square-root $s^{\frac{1}{2}}$ and $(s+\beta)^{\frac{1}{2}}$ are present in (4.1) only in the form of the product $s^{\frac{1}{2}}(s+\beta)^{\frac{1}{2}}$ the branch cuts cancel out each other in $\{s \in \mathbb{C}; -\infty < \mathrm{Re}\{s\} < -\beta; \mathrm{Im}\{s\} = 0\}$, leaving only a branch cut connecting the two branch points as depicted in Fig. 4.1.

Note that by this choice of branch cuts the conditions that $\mathrm{Re}\{\gamma_3^2 + s^{-1}\sigma_3\mu_3\} \geqslant 0$ is also satisfied. Now all singularities present in the inverse Laplace transformations have been identified, the inverse Laplace transform can be determined using

$$\mathcal{L}^{-1}\left\{\hat{R}^n_{2,3}(s)\right\} = \frac{1}{2\pi\mathrm{i}}\int_{s\in\mathrm{Br}} \hat{R}^n_{2,3}\exp(s\kappa)\mathrm{d}s \tag{4.2}$$

where $Br = \{s \in \mathbb{C}; \mathrm{Re}\{s\} = s_0 > 0\}$ denotes the Bromwich path.

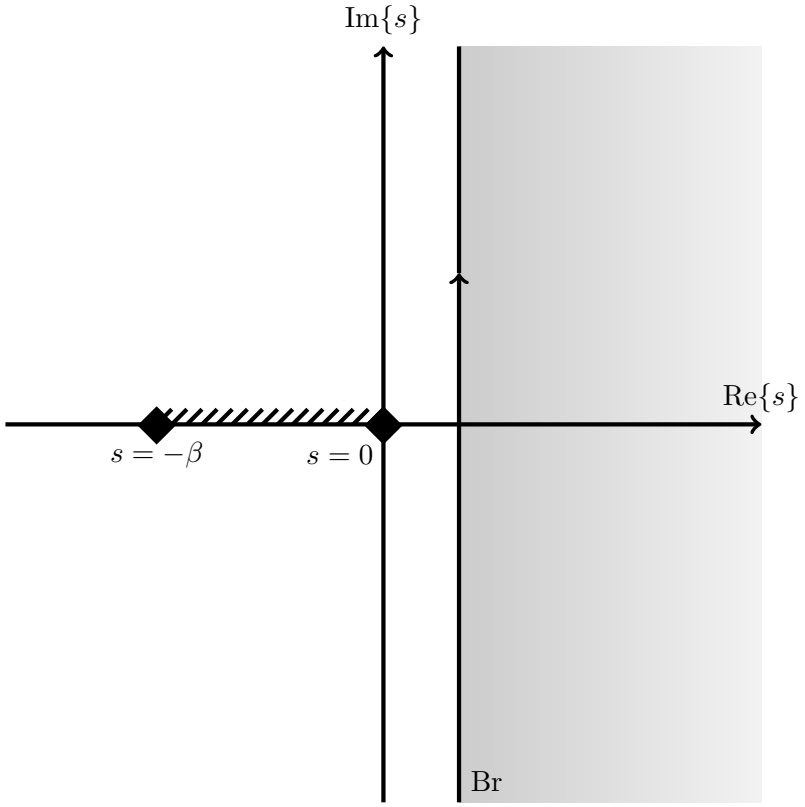

Figure 4.1: Explicative for the choice of the branch cut in (4.2). Br stands for the Bromwich contour.

The instantaneous response of the reflection coefficient $R_0 = \lim_{|s|\to\infty} \hat{R}_{2,3}(s)$ is both added and subtracted in (4.1)

$$\hat{R}^n_{2,3}(s) = R^n_0 + \left[\hat{R}^n_{2,3}(s) - R^n_0\right] = R^n_0 + \hat{R}^n_D(s) \tag{4.3}$$

such that application of Jordan's lemma is valid. Here, $\hat{R}_D(s)$ can be described as the dispersive behavior of $\hat{R}^n_{2,3}(s)$ and is given by

$$\hat{R}^n_{2,3}(s) = \left[\frac{s\gamma_2 - \gamma_3 s^{\frac{1}{2}}\,(s+\beta)^{\frac{1}{2}}}{s\gamma_2 + \gamma_3 s^{\frac{1}{2}}\,(s+\beta)^{\frac{1}{2}}}\right]^n - \left[\frac{\gamma_2 - \gamma_3}{\gamma_2 + \gamma_3}\right]^n. \tag{4.4}$$

Since the first part on the left hand side of (4.3) has no dependence on the Laplace transform parameter s, it is only necessary to determine the inverse Laplace transform of $\hat{R}^n_D(s)$ as

$$R^{(n)}_D(\kappa) = \frac{1}{2\pi \mathrm{i}} \int_{s\in \mathrm{Br}} \hat{R}^n_D \exp(s\kappa)\mathrm{d}s \tag{4.5}$$

where $R^{(n)}_D(\kappa)$ represents the time-domain counterpart of $\hat{R}^n_D$. Please note the superscript on the right hand side of (4.5) which denotes the power of the transform domain function and not an actual power in time-domain.

The contour can now be closed using a semi-circle right of the Bromwich path, the semi-circle's contribution vanishing in the limit $|s| \to \infty$ (Jordan's lemma). Furthermore, since the integrand is analytic for values right of Br, it follows by Cauchy's theorem that $R^{(n)}_D(\kappa) = 0$ for $\kappa < 0$.

Alternatively, the contour can be closed using a semi-circle to the left of the Bromwich path, the semi-circle's contribution vanishing in the limit $|s| \to \infty$ (Jordan's lemma). By Cauchy's theorem

the integration along the Bromwich path can then be replaced by an integration along a contour that encloses the branch cut for $\kappa > 0$.

The contour along the branch cut is obtained by replacing the integration variable s by a new variable ψ such that

$$s = -\frac{\beta}{2} + \frac{\beta}{2}\cos(\psi) = -\frac{\beta}{2}\left[1 - \cos(\psi)\right] \tag{4.6}$$

where $0 < \psi < 2\pi$. From (4.6) it follows that

$$\mathrm{d}s = -\frac{\beta}{2}\sin(\psi)\mathrm{d}\psi \tag{4.7}$$

$$\left[s(s+\beta)\right]^{\frac{1}{2}} = \mathrm{i}\frac{\beta}{2}\sin(\psi). \tag{4.8}$$

Finally, substituting (4.6)-(4.8) in (4.4) and subsequently in (4.5) yields the κ-domain representation (for $\kappa > 0$) of $\hat{R}_D^n(s)$ as

$$\begin{aligned}
R_D^{(n)}(\kappa) &= \frac{1}{2\pi\mathrm{i}}\int_{s\in\mathrm{Br}}\left\{\left[\frac{s\gamma_2 - \gamma_3\left(s(s+\beta)\right)^{\frac{1}{2}}}{s\gamma_2 + \gamma_3\left(s(s+\beta)\right)^{\frac{1}{2}}}\right]^n\right. \\
&\quad \left. - \left[\frac{\gamma_2-\gamma_3}{\gamma_2+\gamma_3}\right]^n\right\}\exp(s\kappa)\mathrm{d}s \\
&= -\frac{1}{2\pi\mathrm{i}}\int_{\psi=0}^{2\pi}\left\{\left[\frac{-\frac{\beta}{2}\left[1-\cos(\psi)\right]\gamma_2 - \gamma_3\mathrm{i}\frac{\beta}{2}\sin(\psi)}{-\frac{\beta}{2}\left[1-\cos(\psi)\right]\gamma_2 + \gamma_3\mathrm{i}\frac{\beta}{2}\sin(\psi)}\right]^n\right. \\
&\quad \left. - \left[\frac{\gamma_2-\gamma_3}{\gamma_2+\gamma_3}\right]^n\right\}\exp\left[-\frac{\beta}{2}\left[1-\cos(\psi)\right]\kappa\right]\frac{\beta}{2}\sin(\psi)\mathrm{d}\psi \\
&= \frac{\beta\mathrm{i}}{4\pi}\int_{\psi=0}^{2\pi}\left\{\left[\frac{\left[1-\cos(\psi)\right]\gamma_2 + \gamma_3\mathrm{i}\sin(\psi)}{\left[1-\cos(\psi)\right]\gamma_2 - \gamma_3\mathrm{i}\sin(\psi)}\right]^n\right. \\
&\quad \left. - \left[\frac{\gamma_2-\gamma_3}{\gamma_2+\gamma_3}\right]^n\right\}\exp\left[-\frac{\beta}{2}\left[1-\cos(\psi)\right]\kappa\right]\sin(\psi)\mathrm{d}\psi.
\end{aligned} \tag{4.9}$$

Please note that in (4.9) the contribution due to the subtraction of the the instantaneous reaction R_0 is zero, since

$$\int_{\psi=0}^{2\pi}\exp\left[-\frac{\beta}{2}\left[1-\cos(\psi)\right]\kappa\right]\sin(\psi)\mathrm{d}\psi = 0 \tag{4.10}$$

which has as a consequence that the instantaneous part can be omitted, yielding

$$\begin{aligned}
R_D^{(n)}(\kappa) = \frac{\beta\mathrm{i}}{4\pi}\int_{\psi=0}^{2\pi}&\left[\frac{\left[1-\cos(\psi)\right]\gamma_2 + \gamma_3\mathrm{i}\sin(\psi)}{\left[1-\cos(\psi)\right]\gamma_2 - \gamma_3\mathrm{i}\sin(\psi)}\right]^n \\
&\exp\left[-\frac{\beta}{2}\left[1-\cos(\psi)\right]\kappa\right]\sin(\psi)\mathrm{d}\psi.
\end{aligned} \tag{4.11}$$

This expression for $R_D^{(n)}(\kappa)$ can then be used to express $\hat{R}_D^n(s)$ as

$$\hat{R}_D^n(s) = \int_{\kappa=0}^{\infty} R_D^{(n)}(\kappa)\exp[-s\kappa]\mathrm{d}\kappa \tag{4.12}$$

which after substitution in (4.3) gives

$$\hat{R}_{2,3}^n(s) = R_0^n + \int_{\kappa=0}^{\infty} R_D^{(n)}(\kappa)\exp[-s\kappa]\mathrm{d}\kappa \tag{4.13}$$

where the s-dependence in this expression occurs in the exponent, only, making it amenable to being employed in the Cagniard-DeHoop method.

In view of a compacter notation, the expression for $\hat{R}^n_{2,3}(s)$ is now rewritten as

$$\begin{aligned}\hat{R}^n_{2,3}(s) &= \int_{\kappa=0}^{\infty} \Big[R^n_0\delta(\kappa) + R^{(n)}_D(\kappa)\Big] \exp[-s\kappa]\mathrm{d}\kappa \\ &= \int_{\kappa=0}^{\infty} \mathcal{R}^{(n)}_{2,3} \exp[-s\kappa]\mathrm{d}\kappa \end{aligned} \tag{4.14}$$

where $\mathcal{R}^{(n)}_{2,3}$ represents the time-domain counterpart of $\hat{R}^n_{2,3}(s)$.

Chapter 5

Determining the space-time expression of the magnetic Hertzian vector potential

This chapter is dedicated to transforming the magnetic Hertzian vector potential back to space-time domain using the Cagniard-DeHoop method. Since the receive antenna will be located in $\mathcal{D}_1$ the focus will be on deriving $u^{\mathrm{T};2,1}(\boldsymbol{X},t)$, the space-time counterpart of the expression of

$$\begin{aligned}\tilde{u}^{\mathrm{T};2,1} = \sum_{n=0}^{\infty}\Bigg\{ &\int_{\kappa=0}^{\infty} \frac{\hat{f}(s)}{2s\gamma_2}\left[1+R_{2,1}\right]R_{2,1}^{n}\mathcal{R}_{2,3}^{(n)}\exp\left[-s(\gamma_1 Z_1+\gamma_2 Z_{2,0}(n)+\kappa)\right]\mathrm{d}\kappa \\ &+\int_{\kappa=0}^{\infty} \frac{\hat{f}(s)}{2s\gamma_2}\left[1+R_{2,1}\right]R_{2,1}^{n}\mathcal{R}_{2,3}^{(n+1)}\exp\left[-s(\gamma_1 Z_1+\gamma_2 Z_{2,1}(n)+\kappa)\right]\mathrm{d}\kappa\Bigg\}\end{aligned} \tag{5.1}$$

in which Z_1, $Z_{2,0}(n)$ and $Z_{2,1}(n)$ represent the propagation distances in the vertical (x_3) direction

$$Z_1 = x_3 - d \tag{5.2}$$

$$Z_{2,0}(n) = [2n+1]\,d - h_{\mathrm{T}} \tag{5.3}$$

$$Z_{2,1}(n) = [2n+1]\,d + h_{\mathrm{T}} \tag{5.4}$$

where n is the number of reflections between the interfaces $\mathcal{I}_{2,1}$ and $\mathcal{I}_{2,3}$. In (5.2)-(5.4) a subscript notation is used wherein the first index denotes the domain and the (possible) second index 0 or 1 is used for waves that propagate upward ($+x_3$) or downward ($-x_3$), respectively, after their generation by the source located at $x_3 = h_{\mathrm{T}}$.

5.1 Application of the inverse Fourier transform

In this section the Laplace domain representation of $\tilde{u}^{\mathrm{T};2,3}$ will be derived by applying the inverse Fourier transform as defined in (1.7). The resulting $\hat{u}^{\mathrm{T};2,3}(\boldsymbol{x},s)$ can then be expressed as

$$\hat{u}^{\mathrm{T};2,1}(\boldsymbol{x},s) = s\hat{f}(s)\left[\hat{g}_0(\boldsymbol{x},s)+\hat{g}_1((x),s)\right] \tag{5.5}$$

where $\hat{g}_0(\boldsymbol{x},s)$ represents the Green's function which describes the contribution of the sum of all waves that propagate in an upward direction after their generation by the source (the first part on the right

hand side of (5.1)). This function is given by

$$\hat{g}_0(\boldsymbol{x},s) = -\sum_{n=0}^{\infty}\frac{1}{8\pi^2}\int_{\alpha_2=-\mathrm{i}\infty}^{\mathrm{i}\infty}\int_{\alpha_1=-\mathrm{i}\infty}^{\mathrm{i}\infty}\int_{\kappa=0}^{\infty}\frac{[1+R_{2,1}]\,R_{2,1}^n\mathcal{R}_{2,3}^{(n)}}{\gamma_2} \exp\left[-s(\alpha_1 x_1+\alpha_2 x_2+\gamma_1 Z_1+\gamma_2 Z_{2,0}(n)+\kappa)\right]\mathrm{d}\kappa\mathrm{d}\alpha_1\mathrm{d}\alpha_2. \tag{5.6}$$

Similarly, $\hat{g}_1(\boldsymbol{x},s)$ represents the Green's function which describes the contribution of the sum of all waves that propagate in a downward direction after the generation by the source (the second part on the right hand side of (5.1)). This function is given by

$$\hat{g}_1(\boldsymbol{x},s) = -\sum_{n=0}^{\infty}\frac{1}{8\pi^2}\int_{\alpha_2=-\mathrm{i}\infty}^{\mathrm{i}\infty}\int_{\alpha_1=-\mathrm{i}\infty}^{\mathrm{i}\infty}\int_{\kappa=0}^{\infty}\frac{[1+R_{2,1}]\,R_{2,1}^n\mathcal{R}_{2,3}^{(n+1)}}{\gamma_2} \exp\left[-s(\alpha_1 x_1+\alpha_2 x_2+\gamma_1 Z_1+\gamma_2 Z_{2,1}(n)+\kappa)\right]\mathrm{d}\kappa\mathrm{d}\alpha_1\mathrm{d}\alpha_2. \tag{5.7}$$

Because of the similarity between (5.6) and (5.7) a compacter notation will be introduced here that is used in the further application of the Cagniard-DeHoop method, as

$$\hat{g}_j(\boldsymbol{x},s) = \sum_{n=0}^{\infty}\hat{g}_{j,n}(\boldsymbol{x},s) \tag{5.8}$$

where

$$\hat{g}_{j,n}(\boldsymbol{x},s) = -\frac{1}{8\pi^2}\int_{\alpha_2=-\mathrm{i}\infty}^{\mathrm{i}\infty}\int_{\alpha_1=-\mathrm{i}\infty}^{\mathrm{i}\infty}\int_{\kappa=0}^{\infty}\hat{G}_{j,n} \exp\left[-s(\alpha_1 x_1+\alpha_2 x_2+\gamma_1 Z_1+\gamma_2 Z_{2,j}(n)+\kappa)\right]\mathrm{d}\kappa\mathrm{d}\alpha_1\mathrm{d}\alpha_2 \tag{5.9}$$

with

$$\hat{G}_{j,n} = \frac{[1+R_{2,1}]\,R_{2,1}^n\mathcal{R}_{2,3}^{(n+j)}}{\gamma_2} \tag{5.10}$$

where $j=0,1$ corresponds to the original subscript of $\hat{g}$ which differentiated between up- and downwards propagating waves after generation by the source. The second subscript in (5.9) denotes the index of reflections of the wave at $\mathcal{I}_{2,1}$.

Therefore, each $\hat{g}_{j,n}$ represents a unique ray that reaches the receiving antenna with $\hat{G}_{j,n}$ denoting the corresponding ray function. This is also referred to as generalized ray.

5.2 Obtaining the general space-time expression

In this section the space-time expression $u^{\mathrm{T};2,1}(\boldsymbol{x},t)$ will be derived. Following the Cagniard-DeHoop method this will be done via a contour deformation such that the Laplace domain Green's function can be written as

$$\hat{g}_{j,n}(\boldsymbol{x},s) = \int_{\tau=\tau_a}^{\infty} g_{j,n}(\boldsymbol{x},\tau)\exp[-s\tau]\mathrm{d}\tau, \quad \text{for } j=0,1; n=1,2,3,.. \tag{5.11}$$

where after substitution in (5.5) the function

$$\hat{u}^{\mathrm{T};2,1}(\boldsymbol{x},s) = s\hat{f}(s)\int_{\tau=\tau_a}^{\infty}\exp[-s\tau]\left[\sum_{n=0}^{\infty}\sum_{j=0}^{1}g_{j,n}(\boldsymbol{x},\tau)\right]\mathrm{d}\tau \tag{5.12}$$

can be recognized as the Laplace transform of

$$u^{\mathrm{T};2,1}(\boldsymbol{x},t)=\int_{\tau=\tau_a}^{t}\partial_{t-\tau}f(t-\tau)\left[\sum_{n=0}^{\infty}\sum_{j=0}^{1}g_{j,n}(\boldsymbol{x},\tau)\right]\mathrm{d}\tau. \tag{5.13}$$

In order to obtain an expression for $\hat{g}_{j,n}(\boldsymbol{x},s)$ as given in (5.11) a Cartesian to cylindrical coordinates transform is employed (see (1.2)-(1.4)) and a change of integration variables $\{\alpha_1,\alpha_2\}\rightarrow\{\omega,q\}$ is performed using the expressions

$$\alpha_1=\omega\cos(\phi)-\mathrm{i}q\sin(\phi) \tag{5.14}$$

$$\alpha_2=\omega\sin(\phi)+\mathrm{i}q\cos(\phi). \tag{5.15}$$

As a result it follows that

$$\mathrm{d}\alpha_1\mathrm{d}\alpha_2=\mathrm{i}\mathrm{d}\omega\mathrm{d}q \tag{5.16}$$

$$\alpha_1^2+\alpha_2^2=\omega^2-q^2 \tag{5.17}$$

$$\alpha_1x_1+\alpha_2x_2=\omega r \tag{5.18}$$

and the functions $\gamma_{1,2,3}$ become

$$\bar{\gamma}_{1,2,3}=\left[\Omega_{1,2,3}^2-\omega^2\right]^{\frac{1}{2}},\quad \mathrm{Re}\{\bar{\gamma}_{1,2,3}\}>0 \tag{5.19}$$

with

$$\Omega_{1,2,3}=\left[q^2+c_{1,2,3}^{-2}\right]^{\frac{1}{2}},\quad \mathrm{Re}\{\Omega_{1,2,3}\}>0. \tag{5.20}$$

Substitution of (5.16)-(5.20) in (5.9) then yields

$$\hat{g}_{j,n}(\boldsymbol{x},s)=-\frac{\mathrm{i}}{8\pi^2}\int_{q=-\infty}^{\infty}\int_{\omega=-\mathrm{i}\infty}^{\mathrm{i}\infty}\int_{\kappa=0}^{\infty}\hat{G}_{j,n}\exp\left[-s(\omega r+\bar{\gamma}_1Z_1+\bar{\gamma}_2Z_{2,j}(n)+\kappa)\right]\mathrm{d}\kappa\mathrm{d}\omega\mathrm{d}q \tag{5.21}$$

where it is noted that $R_{2,1}=R_{2,1}(\bar{\gamma}_1,\bar{\gamma}_2)$ and $R_{2,3}=R_{2,3}(\bar{\gamma}_2,\bar{\gamma}_3)$ in the function $\hat{G}_{j,n}$.

In order to obtain the desired expression (5.11) from (5.21) the integration path of the ω integral is deformed away from the imaginary axis using the parameterization

$$\tau=\omega r+\bar{\gamma}_1Z_1+\bar{\gamma}_2Z_{2,j}(n)+\kappa \tag{5.22}$$

with $\mathrm{Re}\{\tau\}\geqslant 0$ and $\mathrm{Im}\{\tau\}=0$. Furthermore, κ is defined as

$$\kappa=\tau-\xi \tag{5.23}$$

such that after substitution, (5.22) yields

$$\xi=\omega r+\bar{\gamma}_1Z_1+\bar{\gamma}_2Z_{2,j}(n) \tag{5.24}$$

with $T(q)\leqslant\xi<\infty$, where $T(q)$ corresponds to ω_0, i.e. the intersection of the new integration path with the real ω-axis. When (5.24) is solved for ω, one finds two complex conjugate solutions $\omega(\xi)$ and $\omega^*(\xi)$ which together form a new integration path $\mathcal{C}\cup\mathcal{C}^*$.

One has to take into account that the condition imposed on $\gamma_{1,2,3}$ in (5.19) implies the presence of branch-cuts in the ω-plane on the intervals $\{\omega\in\mathcal{C};\min\{\Omega_1,\Omega_2,\Omega_3\}\leqslant|\mathrm{Re}\{\omega\}|<\infty,\mathrm{Im}\{\omega\}=0\}$. When the integration contour $\mathcal{C}\cup\mathcal{C}^*$ intersects the real ω-axis through the branch cut (i.e., if $\omega_0>$

$\min\{\Omega_1, \Omega_2, \Omega_3\}$) the body-wave path, which represents the contribution of the direct ray, has to be supplemented with an additional loop integral along the branch cut. This contribution is denoted as the *head-wave path*.

The minimum value of ξ, $T(q)$, can be found from the first derivative of (5.24) by

$$\partial_\omega \xi = r - \frac{\omega Z_1}{\bar{\gamma}_1} - \frac{\omega Z_{2,j}(n)}{\bar{\gamma}_2} = 0 \tag{5.25}$$

which, when solved for ω, gives $\omega = \omega_0$. By virtue of Snell's law of reflection one can then find that

$$\omega_0 = \Omega_1 \sin(\theta_1) = \Omega_2 \sin(\theta_2) \tag{5.26}$$

with $0 \leqslant \theta_{\min} \leqslant \pi/2$ and $0 \leqslant \theta_i < \theta_{\min}$. Here $\theta_{\min} = \theta_1$ is the angle which corresponds to $\Omega_{\min} = \min\{\Omega_1, \Omega_2\} = \Omega_1$ (since in the examined configuration $c_1 > c_2 > c_3$) and $\theta_i = \theta_2$ is the angle which corresponds to Ω_2. Equation (5.26) ensures that $\max\{\omega_0\} = \Omega_1$. Therefore, the body-wave contour will *never* intersect the real ω-axis on a branch cut and consequently there will be no head-wave contribution in the field in $\mathcal{D}_1$ as depicted in Fig. 5.1.

Note that, since the constant κ is lost when deriving the first derivative with regard to ω of (5.22)

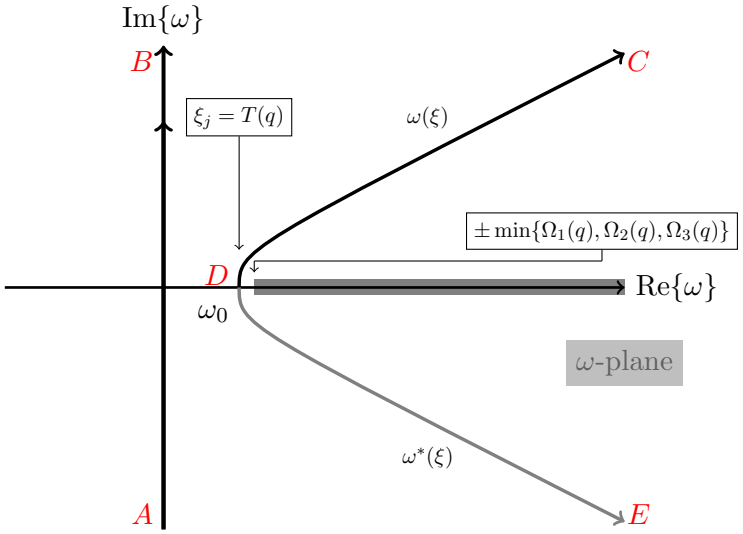

Figure 5.1: The original integration path over the imaginary ω-axis $\{A, B\}$ and the new integration path $\mathcal{C} \cup \mathcal{C}^*$

the function $T(q)$ can be used to determine the minimum value of τ as well.

Now by connecting the original integration path of the ω integral along the imaginary ω-axis with the new path of integration $\mathcal{C} \cup \mathcal{C}^*$ using circular arcs at infinity, a closed contour $\{A, B, C, D, E\}$ is formed. Since the function $\hat{G}_{j,n}$ has no poles it follows from application of Cauchy's theorem that the integral over $\{A, B\}$ is equivalent to the integral over $\{A, E, D, C, B\}$. By using Jordan's Lemma, the contribution of the arcs at infinity vanishes leaving only the integration over the body-wave integration path.

Finally, application of Schwarz's reflection principle yields

$$\hat{g}_{j,n}(\boldsymbol{x}, s) = \frac{1}{8\pi^2} \int_{q=-\infty}^{\infty} \int_{\xi=T(q)}^{\infty} \int_{\tau=\xi}^{\infty} 2\mathrm{Im}\left\{\hat{G}_{j,n}\right\} \partial_\xi \omega(\xi) \partial_\tau \kappa \exp\left[-s\tau\right] \mathrm{d}\tau \mathrm{d}\xi \mathrm{d}q \tag{5.27}$$

where the Jacobian of the mapping from ω to ξ is given by

$$\partial_\xi \omega = \left(r - \frac{\omega Z_1}{\bar{\gamma}_1} - \frac{\omega Z_{2,j}(n)}{\bar{\gamma}_2} \right)^{-1} \tag{5.28}$$

and the Jacobian of the mapping from κ to τ by

$$\partial_\tau \kappa = 1 \tag{5.29}$$

which yields after substitution

$$\hat{g}_{j,n}(\boldsymbol{x}, s) = \frac{1}{8\pi^2} \int_{q=-\infty}^{\infty} \int_{\xi=T(q)}^{\infty} \int_{\tau=\xi}^{\infty} \frac{2\mathrm{Im}\left\{\hat{G}_{j,n}\right\}}{\left(r - \omega Z_1 \bar{\gamma}_1^{-1} - \omega Z_{2,j}(n) \bar{\gamma}_2^{-1}\right)} \exp\left[-s\tau\right] \mathrm{d}\tau \mathrm{d}\xi \mathrm{d}q. \tag{5.30}$$

From interchanging the order of integration it is found that

$$\hat{g}_{j,n}(\boldsymbol{x}, s) = \frac{1}{2\pi^2} \int_{\tau=T(0)}^{\infty} \exp\left[-s\tau\right] \int_{q=0}^{Q(\tau)} \int_{\xi=T(q)}^{\tau} \frac{\mathrm{Im}\left\{\hat{G}_{j,n}\right\}}{r - \omega Z_1 \bar{\gamma}_1^{-1} - \omega Z_{2,j}(n) \bar{\gamma}_2^{-1}} \mathrm{d}\xi \mathrm{d}q \mathrm{d}\tau \tag{5.31}$$

where $q = Q(\tau)$ is the inverse function of $\tau = T(q)$. Note that in (5.31) use was made of the fact that $Q(\tau)$ is an even function of τ. Furthermore it can be seen here that $\tau_a = T(0)$ in (5.13), which represents the arrival time of the ray.

The expression in (5.31) is of the type (5.11) and, consequently, the space-time expression for the Green's function is given by

$$g_{j,n}(\boldsymbol{x}, \tau) = \frac{H(t - T(0))}{2\pi^2} \int_{q=0}^{Q(\tau)} \int_{\xi=T(q)}^{\tau} \frac{\mathrm{Im}\left\{\hat{G}_{j,n}\right\}}{r - \omega Z_1 \bar{\gamma}_1^{-1} - \omega Z_{2,j}(n) \bar{\gamma}_2^{-1}} \mathrm{d}\xi \mathrm{d}q \tag{5.32}$$

with $H(\cdot)$ denoting the Heaviside unit step function.

5.3 Difference between the instantaneous and dispersive response

In Chapter 4 a compacter notation was introduced for the reflection coefficient at $\mathcal{I}_{2,3}$, which allowed to write both the instantaneous and dispersive responses under one Laplace transform. However, the downside of this notation is that in the case of the instantaneous part one extra integral is unnecessarily introduced. Furthermore, since in a numerical evaluation of the integrals it is impossible to handle the Dirac delta function in (4.14) it is at this point better to rewrite the Green's function as the sum of the instantaneous and the dispersive responses.

Firstly, a substitution of the expression for $\mathcal{R}_{2,3}^{(n+j)}$ in (5.10) yields

$$\hat{G}_{j,n} = \delta(\tau - \xi) \hat{G}_{j,n}^{i} + \hat{G}_{j,n}^{d} \tag{5.33}$$

where

$$\hat{G}_{j,n}^{i} = \frac{\left[1 + R_{2,1}\right] R_{2,1}^{n} R_0^{n+j} \delta(\tau - \xi)}{\gamma_2} \tag{5.34}$$

represents the instantaneous response and

$$\hat{G}_{j,n}^{d} = \frac{\left[1 + R_{2,1}\right] R_{2,1}^{n} R_D^{(n+j)}}{\gamma_2} \tag{5.35}$$

represents the dispersive response. Substitution in (5.32) then yields

$$g_{j,n}(\boldsymbol{x},\tau) = g^i_{j,n}(\boldsymbol{x},\tau) + g^d_{j,n}(\boldsymbol{x},\tau) \tag{5.36}$$

where

$$g^i_{j,n}(\boldsymbol{x},\tau) = \frac{H(t-T(0))}{2\pi^2}\int_{q=0}^{Q(\tau)} \frac{\mathrm{Im}\left\{\hat{G}^i_{j,n}\right\}}{r-\omega Z_1\bar{\gamma}_1^{-1}-\omega Z_{2,j}(n)\bar{\gamma}_2^{-1}}\mathrm{d}q \tag{5.37}$$

$$g^d_{j,n}(\boldsymbol{x},\tau) = \frac{H(t-T(0))}{2\pi^2}\int_{q=0}^{Q(\tau)}\int_{\xi=T(q)}^{\tau} \frac{\mathrm{Im}\left\{\hat{G}^d_{j,n}\right\}}{r-\omega Z_1\bar{\gamma}_1^{-1}-\omega Z_{2,j}(n)\bar{\gamma}_2^{-1}}\mathrm{d}\xi\mathrm{d}q. \tag{5.38}$$

Note that due to the Dirac delta function in (5.34) the variable ω in (5.34) and (5.37) is no longer a function of ξ, but a function of τ.

Chapter 6

Determining the space-time expression of the electric and magnetic field components

At this point, an analytic closed-form solution for the magnetic Hertzian vector potential $\mathbf{\Pi}_m(\boldsymbol{X},t)$ has been obtained. This vector potential defines the electric and magnetic field components $\boldsymbol{E}(\boldsymbol{X},t)$ and $\boldsymbol{H}(\boldsymbol{X},t)$ via (3.1) and (3.2). It should, however, be noted that, although $\mathbf{\Pi}_m(X,t)$ was obtained analytically, its determination involves integrals that can only be evaluated numerically. Consequently, the space and time differentiations in (3.1) and (3.2) can only be carried out numerically, this process being known to result in (possibly, very large) errors. It is therefore preferable to carry out the corresponding space/time differentiations in the spectral domain and then perform the relevant space-time inverse transformations. To this end, the components of the electric and magnetic field in $\mathcal{D}_1$ are written out separately in order to determine which variants of the ray functions are needed for determining $\mathbf{\Pi}_m(\boldsymbol{X},t)$. When written out per component, (3.1)-(3.2) give for $\mathcal{D}_1$

$$E_1^{\mathrm{T};2,1} = -\mu_1 \partial_2 \partial_t u^{\mathrm{T};2,1} \tag{6.1}$$

$$E_2^{\mathrm{T};2,1} = \mu_1 \partial_1 \partial_t u^{\mathrm{T};2,1} \tag{6.2}$$

$$E_3^{\mathrm{T};2,1} = 0 \tag{6.3}$$

$$H_1^{\mathrm{T};2,1} = \partial_1 \partial_3 u^{\mathrm{T};2,1} \tag{6.4}$$

$$H_2^{\mathrm{T};2,1} = \partial_2 \partial_3 u^{\mathrm{T};2,1} \tag{6.5}$$

$$H_3^{\mathrm{T};2,1} = \partial_3^2 u^{\mathrm{T};2,1} - \mu_1 \varepsilon_1 \partial_t^2 u^{\mathrm{T};2,1} \tag{6.6}$$

where use was made of the fact that $\mathbf{\Pi}$ has only one non-zero component and that $\sigma_1 = 0$. Furthermore, note that the dependence on $\boldsymbol{X}$ and t have been omitted for compactness.

Subjecting (6.1)-(6.6) to a Laplace transformation with respect to time via (1.5) and a Fourier

transformation with respect to x_1 and x_2 via (1.6) yields

$$\tilde{E}_1^{\mathrm{T};2,1} = \mu_1 s^2 \alpha_2 \tilde{u}^{\mathrm{T};2,1} \tag{6.7}$$

$$\tilde{E}_2^{\mathrm{T};2,1} = -\mu_1 s^2 \alpha_1 \tilde{u}^{\mathrm{T};2,1} \tag{6.8}$$

$$\tilde{E}_3^{\mathrm{T};2,1} = 0 \tag{6.9}$$

$$\tilde{H}_1^{\mathrm{T};2,1} = s^2 \alpha_1 \gamma_1 \tilde{u}^{\mathrm{T};2,1} \tag{6.10}$$

$$\tilde{H}_2^{\mathrm{T};2,1} = s^2 \alpha_2 \gamma_1 \tilde{u}^{\mathrm{T};2,1} \tag{6.11}$$

$$\tilde{H}_3^{\mathrm{T};2,1} = s^2 \left(\gamma_1^2 - \mu_1 \varepsilon_1\right) \tilde{u}^{\mathrm{T};2,1} \tag{6.12}$$

where it has been used that $\partial_t \to s$ under the Laplace transformation and $\partial_{1,2} \to -s\alpha_{1,2}$ under the Fourier transformation. Furthermore, from the definition of $\tilde{u}^{\mathrm{T};2,1}$ in (3.22) it follows that

$$\partial_3 \tilde{u}^{\mathrm{T};2,1} = -s\gamma_1 \tilde{u}^{\mathrm{T};2,1}. \tag{6.13}$$

It is now noted that for any function $f(t)$ admitting a Laplace transform $\mathcal{L}^{-1}\left\{s^m \hat{f}(s)\right\} = \partial_t^m f(t)$, for $m \in \mathbb{Z}$.

6.1 Application of the Cagniard-deHoop method for the electric field

From (6.7)-(6.8) it is found that the determination of the electric field strength components require manipulating expressions containing the terms $s^2\alpha_1\tilde{u}^{\mathrm{T};2,1}$ or $s^2\alpha_2\tilde{u}^{\mathrm{T};2,1}$. Using the same method as in the case of the vector potential, the electric field components can, after application of the inverse Fourier transform, be written as

$$\hat{E}_p^{\mathrm{T};2,1} = (-1)^{p-1}\mu_1 s^3 \hat{f}(s) \sum_{n=0}^{\infty}\sum_{j=0}^{1} \hat{m}_{j,n}^E(\boldsymbol{x}, s, p), \quad p = \{1, 2\} \tag{6.14}$$

with

$$\begin{aligned}\hat{m}_{j,n}^E(\boldsymbol{x}, s, p) = -\frac{\mathrm{i}}{8\pi^2} \int_{q=-\infty}^{\infty} \int_{\omega=-\mathrm{i}\infty}^{\mathrm{i}\infty} \int_{\kappa=0}^{\infty} \hat{M}_{j,n}^E(\omega, q, p) \\ \exp\left[-s(\omega r + \bar{\gamma}_1 Z_1 + \bar{\gamma}_2 Z_{2,j}(n) + \kappa)\right] \mathrm{d}\kappa \mathrm{d}\omega \mathrm{d}q\end{aligned} \tag{6.15}$$

where the function $\hat{M}_{j,n}^E(\omega, q, p)$ in the integrand is given by

$$\begin{aligned}\hat{M}_{j,n}^E(\omega, q, p) &= \alpha_{\varsigma(p)} \hat{G}_{j,n} \\ &= \frac{\alpha_{\varsigma(p)}}{\gamma_2} \left[1 + R_{2,1}\right] R_{2,1}^n \mathcal{R}^{(n+j)}\end{aligned} \tag{6.16}$$

where

$$\varsigma(p) = \begin{cases} 2 & \text{for } p = 1 \\ 1 & \text{for } p = 2 \end{cases}. \tag{6.17}$$

Following the Cagniard-deHoop method the integral along the ω-axis is again deformed away from the imaginary axis using (5.22). However, it is noted that in this case (6.15) does not meet the requirements

necessary for the application of Jordan's Lemma, as (6.16) does not go to zero for $\omega \to \infty$ due to the multiplication by $\alpha_{1,2}$. To address this, (6.15) is written as

$$\hat{m}^E_{j,n}(\boldsymbol{x},s,p) = \frac{\mathrm{d}}{\mathrm{d}s}\left[\frac{\mathrm{i}}{8\pi^2}\int_{q=-\infty}^{\infty}\int_{\omega=-\mathrm{i}\infty}^{\mathrm{i}\infty}\int_{\kappa=0}^{\infty}\frac{\hat{M}^E_{j,n}(\omega,q,p)}{(\omega r+\bar{\gamma}_1 Z_1+\bar{\gamma}_2 Z_{2,j}(n)+\kappa)}\right.$$
$$\left.\exp\left[-s(\omega r+\bar{\gamma}_1 Z_1+\bar{\gamma}_2 Z_{2,j}(n)+\kappa)\right]\mathrm{d}\kappa\mathrm{d}\omega\mathrm{d}q\right] \tag{6.18}$$

where both an integration and a differentiation with respect to s have been applied. In this manner, the condition

$$\left|\frac{\hat{M}^E_{j,n}(\omega,q,p)}{(\omega r+\bar{\gamma}_1 Z_1+\bar{\gamma}_2 Z_{2,j}(n)+\kappa)}\right| \to 0, \quad \text{as } \omega\to\infty \tag{6.19}$$

is met that, in turn, implies enforcing the function under the integral now fulfills the requirements for the application of Jordan's lemma. The integration along the imaginary ω-axis can then be replaced by an integral along the Cagniard-deHoop contour $\mathcal{C}\cup\mathcal{C}^*$. Note that the integration with respect to s has introduced a pole at $\tau = \omega r+\bar{\gamma}_1 Z_1+\bar{\gamma}_2 Z_{2,j}(n)+\kappa = 0$ which needs to be taken into account during the deformation. However, the contribution of this pole to the integral is zero, as shown in Appendix A.

Another consequence of the multiplication by $\alpha_{1,2}$ is that the function in the integrand in (6.18) is not anymore an even function in q. Therefore, care must be taken with the integration with respect to q, since this integral can no longer be replaced by two times an integral over the interval $0 \leqslant q < \infty$. Note that the ω term disappears in α_1 for $\phi = -\frac{\pi}{2}, \frac{\pi}{2}$ (see (5.14)) and α_2 for $\phi = 0, \pi$ (see (5.15)). In those cases the integrand in (6.18) is an odd function in q, yielding a zero integral. As a consequence $E_1^{\mathrm{T};2,1}$ becomes zero for $\phi = 0, \pi$ and $E_2^{\mathrm{T};2,1}$ becomes zero for $\phi = -\frac{\pi}{2}, \frac{\pi}{2}$. This observation is in line with the radiation characteristics of a magnetic dipole in a configuration which is invariant in the x_1 and x_2 directions [5, Sec 26.9 and 26.10].

After deforming the integral along the imaginary ω-axis and rearranging the order of integration, $\hat{m}^E_{j,n}$ becomes

$$\hat{m}^E_{j,n}(\boldsymbol{x},s,p) = \frac{\mathrm{d}}{\mathrm{d}s}\left[\frac{-1}{4\pi^2}\int_{\tau=T(0)}^{\infty}\exp[-s\tau]\int_{q=-Q(\tau)}^{Q(\tau)}\int_{\xi=T(q)}^{\tau}\right.$$
$$\left.\mathrm{Im}\left\{\frac{\hat{M}^E_{j,n}(\omega,q,p)}{(r-\omega Z_1\bar{\gamma}_1^{-1}-\omega Z_{2,j}(n))\tau}\right\}\mathrm{d}\xi\mathrm{d}q\mathrm{d}\tau\right] \tag{6.20}$$

which can be recognized as the Laplace transform of

$$m^E_{j,n}(\boldsymbol{x},\tau,p) = \frac{tH(t-T(0))}{4\pi^2}\int_{q=-Q(\tau)}^{Q(\tau)}\int_{\xi=T(q)}^{\tau}\mathrm{Im}\left\{\frac{\hat{M}^E_{j,n}(\omega,q,p)}{(r-\omega Z_1\bar{\gamma}_1^{-1}-\omega Z_{2,j}(n))\tau}\right\}\mathrm{d}\xi\mathrm{d}q. \tag{6.21}$$

Finally, the space-time expression for the electric field components is given by

$$E_p^{\mathrm{T};2,1}(\boldsymbol{x},t) = \int_{\tau=\tau_a}^{t}\partial^3_{t-\tau}f(t-\tau)\left[\sum_{n=0}^{\infty}\sum_{j=0}^{1}m^E_{j,n}(\boldsymbol{x},\tau)\right]\mathrm{d}\tau. \tag{6.22}$$

6.2 Application of the Cagniard-deHoop method for the magnetic field

From (6.10)-(6.12) it is found that the determination of the magnetic field strength components require manipulating expressions containing the terms $s^2\alpha_1\gamma_1\tilde{u}^{\mathrm{T};2,1}$, $s^2\alpha_2\gamma_1\tilde{u}^{\mathrm{T};2,1}$ or $s^2\left(\gamma_1^2-\mu_1\varepsilon_1\right)\tilde{u}^{\mathrm{T};2,1}$. Here

the same approach will be followed as in the previous section. After application of the inverse Fourier transform, (6.10)-(6.12) yield

$$\hat{H}_1^{\mathrm{T};2,1} = s^3 \hat{f}(s) \sum_{n=0}^{\infty} \sum_{j=0}^{1} \hat{m}_{j,n}^{H}(\boldsymbol{x}, s, p) \tag{6.23}$$

with

$$\hat{m}_{j,n}^{H}(\boldsymbol{x}, s, p) = -\frac{\mathrm{i}}{8\pi^2} \int_{q=-\infty}^{\infty} \int_{\omega=-\mathrm{i}\infty}^{\mathrm{i}\infty} \int_{\kappa=0}^{\infty} \hat{M}_{j,n}^{H}(\omega, q, p) \exp\left[-s(\omega r + \bar{\gamma}_1 Z_1 + \bar{\gamma}_2 Z_{2,j}(n) + \kappa)\right] \mathrm{d}\kappa \mathrm{d}\omega \mathrm{d}q \tag{6.24}$$

where the functions $\hat{M}_{j,n}^{H}(\omega, q, p)$ in the integrand are given by

$$\hat{M}_{j,n}^{H}(\omega, q, 1) = \alpha_1 \bar{\gamma}_1 \hat{G}_{j,n} \tag{6.25}$$

$$\hat{M}_{j,n}^{H}(\omega, q, 2) = \alpha_2 \bar{\gamma}_1 \hat{G}_{j,n} \tag{6.26}$$

$$\hat{M}_{j,n}^{H}(\omega, q, 3) = \left(\bar{\gamma}_1^2 - \mu_1 \varepsilon_1\right) \hat{G}_{j,n}. \tag{6.27}$$

Following the Cagniard-deHoop method the integral along the ω-axis is again deformed away from the imaginary axis using (5.22), but again, in this case Jordan's lemma does not apply due to the multiplication with either $\alpha_1\gamma_1$, $\alpha_2\gamma_2$ or $(\gamma_1^2 - \mu_1\varepsilon_1)$. To address this, (6.24) needs to be integrated and differentiated with respect to s twice. Note that as a result the pole at $\tau = \omega r + \bar{\gamma}_1 Z_1 + \bar{\gamma}_2 Z_{2,j}(n) + \kappa = 0$ that is introduced as a result of the integration is now of order 2. However, the contribution of this pole to the integral is zero, as shown in Appendix A.

Furthermore, care must be taken that the magnetic field components $H_1^{\mathrm{T};2,1}$ and $H_2^{\mathrm{T};2,1}$ are not anymore even functions in q as a result of multiplication with $\alpha_{1,2}$. Similar to the electric field components, this has the consequence that $H_1^{\mathrm{T};2,1}$ becomes zero for $\phi = -\frac{\pi}{2}, \frac{\pi}{2}$ and that $H_2^{\mathrm{T};2,1}$ becomes zero for $\phi = 0, \pi$. Note that $H_3^{\mathrm{T};2,1}$ remains an even function in q and is therefore independent of ϕ. Again, this observation is in line with the radiation characteristics of a magnetic dipole in a configuration which is invariant in the x_1 and x_2 directions.

Application of double integration and differentiation with respect to s in (6.24) then yields the function

$$\hat{m}_{j,n}^{H}(\boldsymbol{x}, s, p) = \frac{\mathrm{d}^2}{\mathrm{d}s^2} \left[\frac{-\mathrm{i}}{8\pi^2} \int_{q=-\infty}^{\infty} \int_{\omega=-\mathrm{i}\infty}^{\mathrm{i}\infty} \int_{\kappa=0}^{\infty} \frac{\hat{M}_{j,n}^{H}(\omega, q, p)}{(\omega r + \bar{\gamma}_1 Z_1 + \bar{\gamma}_2 Z_{2,j}(n) + \kappa)^2} \exp\left[-s(\omega r + \bar{\gamma}_1 Z_1 + \bar{\gamma}_2 Z_{2,j}(n) + \kappa)\right] \mathrm{d}\kappa \mathrm{d}\omega \mathrm{d}q \right] \tag{6.28}$$

which fulfills the requirements for the application of Jordan's lemma. The integration along the imaginary ω axis can be replaced by an integral along the Cagniard-deHoop contour $\mathcal{C} \cup \mathcal{C}^*$. Rearranging the order of integration then yields

$$\hat{m}_{j,n}^{H}(\boldsymbol{x}, s, p) = \frac{\mathrm{d}^2}{\mathrm{d}s^2} \left[\frac{1}{4\pi^2} \int_{\tau=T(0)}^{\infty} \exp[-s\tau] \int_{q=-Q(\tau)}^{Q(\tau)} \int_{\xi=T(q)}^{\tau} \mathrm{Im}\left\{ \frac{\hat{M}_{j,n}^{H}(\omega, q, p)}{(r - \omega Z_1 \bar{\gamma}_1^{-1} - \omega Z_{2,j}(n))\tau^2} \right\} \mathrm{d}\xi \mathrm{d}q \mathrm{d}\tau \right] \tag{6.29}$$

which can be recognized as the Laplace transform of

$$m_{j,n}^{H}(\boldsymbol{x}, \tau, p) = \frac{t^2 H(t - T(0))}{4\pi^2} \int_{q=-Q(\tau)}^{Q(\tau)} \int_{\xi=T(q)}^{\tau} \mathrm{Im}\left\{ \frac{\hat{M}_{j,n}^{H}(\omega, q, p)}{(r - \omega Z_1 \bar{\gamma}_1^{-1} - \omega Z_{2,j}(n))\tau^2} \right\} \mathrm{d}\xi \mathrm{d}q. \tag{6.30}$$

Finally, the space-time expression for the electric field components is then given by

$$H_p(\boldsymbol{x},t) = \int_{\tau=\tau_a}^{t} \partial_{t-\tau}^3 f(t-\tau) \left[\sum_{n=0}^{\infty} \sum_{j=0}^{1} m_{j,n}(\boldsymbol{x},\tau) \right] \mathrm{d}\tau. \tag{6.31}$$

Chapter 7

Numerical implementation

This chapter will discuss the steps involved by the numerical implementation of the evaluation of the Green's functions. These are the Green's function of the instantaneous response (5.37) as

$$g^i_{j,n} = \frac{H(t-T(0))}{2\pi^2}\int_{q=0}^{Q(\tau)} \frac{\mathrm{Im}\{\hat{M}^i_{j,n}\}}{r-\omega Z_1\bar{\gamma}_1^{-1}-\omega Z_2(n)\bar{\gamma}_2^{-1}}\mathrm{d}q \tag{7.1}$$

and the Green's function of the dispersive response (5.38) as

$$g^d_{j,n} = \frac{H(t-T(0))}{2\pi^2}\int_{q=0}^{Q(\tau)}\int_{\xi=T(q)}^{\tau} \frac{\mathrm{Im}\{\hat{M}^i_{j,n}\}}{r-\omega Z_1\bar{\gamma}_1^{-1}-\omega Z_2(n)\bar{\gamma}_2^{-1}}\mathrm{d}\xi\mathrm{d}q. \tag{7.2}$$

These steps include the calculation of the function $T(q)$ and its inverse function $Q(\tau)$, which are used to determine the boundaries of the integrals. Subsequently, the determination of the values on the contour $\omega(\tau)$ will be discussed, including its first derivative which occurs in the expression of the Jacobian. Finally it is discussed per integral how singularities are dealt with and which numerical integration method is employed.

7.1 Determination of the arrival time as a function of q

The function $T(q)$ represents the minimum value of ξ (and τ) and the corresponding value of ω_0 represents the intersection of the contour $\mathcal{C}\cup\mathcal{C}^*$ with the real ω-axis, as already discussed in section 5.2. Recall that an alternative manner of determining ω_0 was by using Snell's law (see (5.26)).

There, it has also been mentioned that this value of ω_0 can be found using Snell's law as given by (5.26). This implies determining the quantities $\sin(\theta_1)$ and $\sin(\theta_2)$ that in turn will yield the intersection point of the ray with $\mathcal{I}_{2,1}$. To begin with

$$\sin(\theta_1) = \frac{Z_1}{\left[r_1^2+Z_1^2\right]^{\frac{1}{2}}} \tag{7.3}$$

$$\sin(\theta_2) = \frac{Z_{2,j}(n)}{\left[r_2^2+Z_{2,j}^2(n)\right]^{\frac{1}{2}}} \tag{7.4}$$

see Fig. 7.1. Substituting $r_2 = r - r_1$ and subsequently squaring both sides, one then finds a quartic function which can be solved to find four possible values for r_1, one of which denotes the horizontal distance between the source and the intersection point with $\mathcal{I}_{2,1}$.

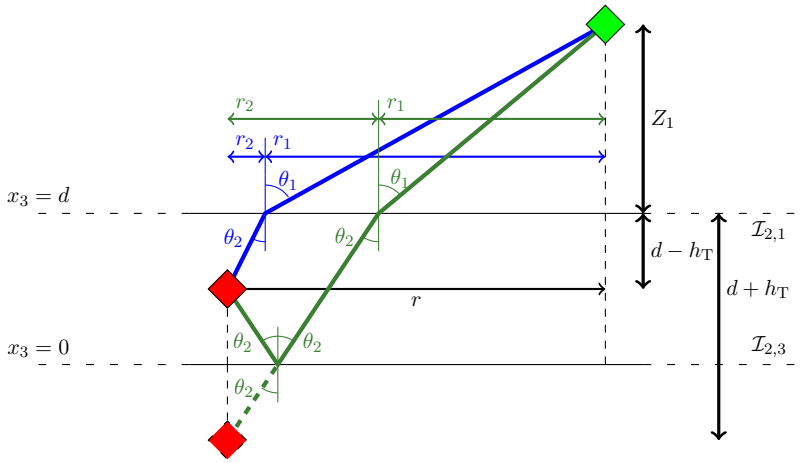

Figure 7.1: Example for two rays (blue for $\{j, n\} = \{0, 0\}$ and green for $\{j, n\} = \{1, 0\}$) to illustrate the point of intersection with $\mathcal{I}_{2,1}$

Since ω_0 represents a minimum value of τ one could also employ an iterative root finding method to find $\partial_\omega \tau = 0$ as given by

$$\partial_\omega \tau = r - \omega \bar{\gamma}_1^{-1} Z_1 - \omega \bar{\gamma}_2^{-1} Z_{2,j}(n) = 0. \tag{7.5}$$

Since there is no head-wave contribution in $\mathcal{D}_1$ it is guaranteed that $0 < \omega_0 < \Omega_{min}$. Following [22] it can be shown that the derivative of (7.5)

$$\partial_\omega^2 \tau = -\left(\Omega_1^2 \bar{\gamma}_1^{-3} Z_1 + \Omega_2^2 \bar{\gamma}_2^{-3} Z_{2,j}(n)\right) < 0, \quad \text{for } 0 < \omega_0 < \Omega_{min}. \tag{7.6}$$

Therefore, (7.5) is monotonous for $\{0 < \mathrm{Re}\{\omega\} < \Omega_{min}, \mathrm{Im}\{\omega\} = 0\}$, which implies that there is at most one ω for which $\partial_\omega \tau = 0$ in this interval.

It was found in Section 5.2 from Snell's law that ω_0 is at most equal to Ω_1 (i.e. $\max\{\omega_0\} = \Omega_1$). Via (5.19) it is found that the propagation factor yields $\bar{\gamma}_1 = 0$ for $\omega_0 = \Omega_1$. This, in turn, result in division by zero through $\bar{\gamma}_1^{-1}$ in (7.5) and (7.6). Even though the value of ω_0 does not necessarily have to be Ω_1 (in fact, note from Fig. 7.1 that this only happens when $d - h_\mathrm{T} = 0$) it can happen that this value does occur during the iterative process. As a result, an iterative method such as Newton's method cannot be used.

As an alternative, the regula falsi or false positioning method is implemented in this thesis. This method has also been suggested and implemented in [6, 20, 22]. In short, the regula falsi method uses two points ω_A and ω_B such that $\partial_\omega \tau(\omega_A) > 0$ and $\partial_\omega \tau(\omega_B) < 0$. At each iteration, the intersection between the secant line through $(\omega_A, \partial_\omega \tau(\omega_A))$ and $(\omega_B, \partial_\omega \tau(\omega_B))$ and the ω-axis, i.e. ω_C, is determined. If the absolute value of $\partial_\omega \tau(\omega_C)$ is smaller than some tolerance value, the algorithm is terminated and $\omega_0 = \omega_C$. If not, ω_C is taken in the following iteration as the new value for either ω_A (if $\partial_\omega \tau(\omega_C) > 0$) or ω_B (if $\partial_\omega \tau(\omega_C) < 0$). Since there is only one solution for ω_0 on the interval $\{0 < \mathrm{Re}\{\omega\} < \Omega_{min}, \mathrm{Im}\{\omega\} = 0\}$, the choice for ω_A and ω_B is arbitrary as long as they fulfill the conditions of having opposite signs. One possibility is to use $\omega_A = 0$ and $\omega_B = \Omega_\mathrm{min} = \Omega_1$, [20].

It should be observed that this procedure does not preclude the potential occurrence of divisions by zero. To address this, [6, 22] introduced a slight modification of the choice for end-points to be used in the *regula falsi* method, by accounting for two auxiliary functions $a_A(\omega)$ and $a_B(\omega)$ that satisfy the condition

$$a_A(\omega) < \partial_\omega \tau < a_B(\omega) \tag{7.7}$$

and have analytic solutions ω_A and ω_B at $a_{A,B} = 0$, respectively. Following [22], the auxiliary functions

are selected as

$$a_A(\omega) = r - \frac{\omega}{\bar{\gamma}_{\min}} \left(Z_1 + Z_{2,j}(n)\right) \tag{7.8}$$

$$a_B(\omega) = r - \frac{\omega}{\bar{\gamma}_{\min}} Z_{\min} \tag{7.9}$$

where $\bar{\gamma}_{\min}$ and $Z_{\min}$ are the propagation factor and vertical distance that correspond to $\mathcal{D}_1$, since $\Omega_{\min} = \Omega_1$. Therefore, $\bar{\gamma}_{\min} = \bar{\gamma}_1$ and $Z_{\min} = Z_1$ in (7.8) and (7.9). With these choices, the solutions ω_A and ω_B are

$$\omega_A = \Omega_1 \frac{r}{\left[r^2 + (Z_1 + Z_{2,j}(n))^2\right]^{\frac{1}{2}}} \tag{7.10}$$

$$\omega_B = = \Omega_1 \frac{r}{\left[r^2 + Z_1^2\right]^{\frac{1}{2}}} \tag{7.11}$$

with Z_1 and $\bar{\gamma}_1$ being already substituted. The solutions ω_A and ω_B are now taken as the limits of the search interval for the application of the *regula falsi*. From (7.10) and (7.11) it is obvious that $\omega = \Omega_1$, that would lead to a division by zero, is outside the search interval and, consequently, any possible division by zero during the iterative process is prevented. Moreover, the chosen initial search interval being quite small increases the effectiveness of the employed iterative scheme.

7.2 Determination of upper boundary of the integral with respect to q as a function of τ

Recall that $Q(\tau)$ is defined as the function which returns a value for q such that $T(q) = \tau$. Therefore an iterative root-finding algorithm such as Newton's method can be used to find the root of a function $f(q)$, using its first derivative with regard to q as

$$f(q) = T(q) - \tau \tag{7.12}$$

$$\partial_q f(q) = q \left(\frac{Z_1}{\bar{\gamma}_1} + \frac{Z_{2,j}(n)}{\bar{\gamma}_2} \right) \tag{7.13}$$

which are used to update the value of q using the formula

$$q^{\text{new}} = q^{\text{old}} - \frac{f(q^{\text{old}})}{\partial_q f(q^{\text{old}})} \tag{7.14}$$

where q^{old} is the value q from either the previous iteration or the initial value (when it is the first iteration). The initial value of q is taken as the analytical solution with regard to q for

$$\omega r + \bar{\gamma}_{\min} \left(Z_1 + Z_{2,j}(n)\right) = 0 \tag{7.15}$$

which is given by

$$q = \left[\frac{\tau^2}{(r^2 + (Z_1 + Z_{2,j}(n))^2)} - \frac{1}{c_1^2} \right]^{\frac{1}{2}} . \tag{7.16}$$

When the absolute value of $f(q)$ becomes smaller than some tolerance, the algorithm is terminated and $Q(\tau) = q$.

7.3 Determination of the values on the Cagniard-deHoop contour

This section will discuss an analytical and a numerical method to determine the values for ω along the Cagniard-deHoop contour as a function of either τ or ξ. Note that, from Section 5.3 it follows that the τ (in (7.1)) and ξ (in (7.2)) as a function of ω are identical, given by

$$\xi = \tau = \omega r + \bar{\gamma}_1 Z_1 + \bar{\gamma}_2 Z_{2,j}(n). \tag{7.17}$$

from which it follows that the same method can be used in both cases. Arbitrarily, ξ has been chosen for this section.

In order to solve (7.17) analytically for ω, both sides are squared twice as

$$\left[(\xi - \omega r)^2 - \left(\bar{\gamma}_1^2 Z_1^2 + \bar{\gamma}_2^2 Z_{2,j}^2(n)\right)\right]^2 = 4\bar{\gamma}_1^2\bar{\gamma}_2^2 Z_1^2 Z_{2,j}^2(n) \tag{7.18}$$

which yields a quartic function for ω as

$$A\omega^4 + B\omega^3 + C\omega^2 + D\omega + E = 0 \tag{7.19}$$

where

$$A = r^4 + \left(Z_1^2 - Z_{2,j}^2(n)\right) + 2r^2\left(Z_1^2 + Z_{2,j}^2(n)\right) \tag{7.20}$$

$$B = -4\xi r^3 - 4\xi r\left(Z_1^2 + Z_{2,j}^2(n)\right) \tag{7.21}$$

$$\begin{aligned} C = {} & 6\xi^2 r^2 - 2\left[\left(Z_1^2 - Z_{2,j}^2(n)\right)\left(\Omega_1^2 Z_1^2 - \Omega_2^2 Z_{2,j}^2(n)\right)\right] \\ & + 2\xi^2\left(Z_1^2 + Z_{2,j}^2(n)\right) - 2r^2\left(\Omega_1^2 Z_1^2 + \Omega_2^2 Z_{2,j}^2(n)\right) \end{aligned} \tag{7.22}$$

$$D = -4\xi^3 r + 4\xi r\left(\Omega_1^2 Z_1^2 + \Omega_2^2 Z_{2,j}^2(n)\right) \tag{7.23}$$

$$E = \xi^4 + \left(\Omega_1^2 Z_1^2 - \Omega_2^2 Z_{2,j}^2(n)\right)^2 - 2\xi^2\left(\Omega_1^2 Z_1^2 + \Omega_2^2 Z_{2,j}^2(n)\right) \tag{7.24}$$

which can be solved using Cardano's formula. However, inherent to the nature of a quartic function, this method returns four solutions. As expected, two of these solutions will be the mutual conjugate values which form $\mathcal{C} \cup \mathcal{C}^*$. In order to narrow down the set of solutions one can use the knowledge that the solution belonging to the Cagniard-DeHoop contour lies in the first quadrant (i.e. $\mathrm{Re}\{\omega\} > 0$, $\mathrm{Im}\{\omega\} \geqslant 0$), but it can not be guaranteed that only one solution will satisfy this condition.

Therefore it may be more advantageous to employ an iterative root finding method such as Newton's method,using

$$f(\omega) = \omega r + \bar{\gamma}_1 Z_1 + \bar{\gamma}_2 Z_{2,j}(n) - \xi \tag{7.25}$$

$$\partial_\omega f(\omega) = r - \omega\bar{\gamma}_1^{-1} Z_1 - \omega\bar{\gamma}_2^{-1} Z_{2,j}(n) \tag{7.26}$$

where it is noted that $\partial_\omega f(\omega) = (\partial_\xi \omega)^{-1}$ (and, subsequently, also $(\partial_\tau \omega)^{-1}$) Therefore the Jacobian (5.28) is found as by product of Newton's method. Furthermore, the Newton's method is unbounded when $\xi = T(q)$. However, since at this point the value of ω is already known this value does not need to be calculated.

The initial value is determined following the method in [4]. This yields for the initial value of ω

$$\omega = \frac{r\xi + \mathrm{i}(Z_1 + Z_{2,j}(n))\left[\xi^2 - (r^2 + (Z_1 + Z_{2,j}(n))^2)\left(\frac{Z_1\Omega_1 + Z_{2,j}(n)\Omega_2}{Z_1 + Z_{2,j}(n)}\right)\right]^{\frac{1}{2}}}{r^2 + (Z_1 + Z_{2,j}(n))^2} \tag{7.27}$$

which takes into account not only the asymptotic behavior of ω as $\xi \to \infty$, but also its behavior near the real ω-axis. When the absolute value of $f(\omega)$ becomes smaller than some tolerance value, the algorithm is terminated and $\omega(\xi) = \omega$.

Although the iterative solution offers the benefit of convergence to a single solution, it has a considerably higher computation time due Matlab being a interpreted programming language. Since it is not a priori clear which solution from Cardano's formula is a needed one, experiments with an iterative solution have been conducted. These experiments have shown that the Cardano solution in the first quadrant with the least absolute value is the needed one. Consequently this choice was henceforth used in the code.

7.4 Coordinate stretching of the integrals

Both integrals (7.1) and (7.2) have a Jacobian as a result of the change the variables from τ to ω or from ξ to ω, respectively. This Jacobian has already been found to be the inverse of $\partial_{\tau,\xi}\omega$, which is by definition zero for $\omega = \omega_0$ (7.5). As a consequence, the integral in (7.1) has a singularity at its end point $q = Q(\tau)$, whereas the integral in (7.2) has a singularity at its starting point $\xi = T(q)$. In this section, a variable stretching procedure is introduced for handling the end-point singularities.

7.4.1 Stretching of the initial part of the Green's function

The integral with respect to q is stretched by introducing a new variable v such that

$$q = Q(\tau)\cos(v) \tag{7.28}$$

for $0 < v < \pi/2$. This new variable v is then interchanged for q by using the Jacobian

$$\partial_v q = -\left[Q^2(\tau) - q^2\right]^{\frac{1}{2}} \tag{7.29}$$

which, after substitution in (7.1), gives

$$g^i_{j,n} = \frac{U(t-T(0))}{2\pi^2}\int_{v=0}^{\pi/2} \frac{\mathrm{Im}\{\hat{M}^i_{j,n}\}}{r - \omega Z_1 \bar{\gamma}_1^{-1} - \omega Z_2(n)\bar{\gamma}_2^{-1}}\left[Q^2(\tau) - q^2\right]^{\frac{1}{2}}\mathrm{d}v. \tag{7.30}$$

The integral in (7.30) is implemented using an adaptive quadrature rule based on the Lobatto quadrature.

7.4.2 Stretching of the dispersive part of the Green's function

The integral with respect to variable ξ is stretched by introducing a new variable ψ such that

$$\xi = \left[T^2(q)\cos^2(\psi) + \tau^2\sin^2(\psi)\right]^{\frac{1}{2}} \tag{7.31}$$

for $0 < \psi < \pi/2$. This new variable ψ is then interchanged for ξ by using the Jacobian

$$\partial_\psi \xi = \left[\frac{(\tau^2 - T^2(q))\cos(\psi)\sin(\psi)}{T^2(q)\cos^2(\psi) + \tau^2\sin^2(\psi)}\right]^{\frac{1}{2}} \tag{7.32}$$

which, after substitution in (7.2), gives

$$g^d_{j,n} = \frac{U(t-T(0))}{2\pi^2}\int_{q=0}^{Q(\tau)}\int_{\psi=0}^{\pi/2} \frac{\mathrm{Im}\{\hat{M}^i_{j,n}\}}{r - \omega Z_1 \bar{\gamma}_1^{-1} - \omega Z_2(n)\bar{\gamma}_2^{-1}} \left[\frac{(\tau^2 - T^2(q))\cos(\psi)\sin(\psi)}{T^2(q)\cos^2(\psi) + \tau^2\sin^2(\psi)}\right]^{\frac{1}{2}} \mathrm{d}\psi\mathrm{d}q. \tag{7.33}$$

The variable stretching procedure as described above deviates from the described method in 7.4.1 in the sense that it stretches for both end-points of the integral, whereas the latter only stretches for one end-point. The main reason for this lies with the fixed end-points of the integral ψ. This allows for a vectorized solution of the integrand which can subsequently be integrated using the trapezoidal rule, which amounts to a decrease in the computation time in Matlab.

For the integration with regard to the variable q an adaptive quadrature rule based on the Lobatto quadrature is used, as was also the case with the initial part of the Green's function.

Chapter 8

Numerical results

8.1 The source signature

The numerical result presented in this chapter are (almost) all excited by the same pulsed current through the transmit antenna. For the derivation of the magnetic Hertzian potential, as well as for electric and magnetic field components the source signature has been defined as the magnetic moment of the transmitting loop. The magnetic moment $f(t)$ relates to the induced current as

$$f(t) = I^T(t) A^T \boldsymbol{i}_3 \tag{8.1}$$

where $I^T(t)$ represents the current as a function of time and $A\boldsymbol{i}_3$ represent the vectorial area of the transmit loop antenna.

The excitation of the current loop is taken to be a monocycle pulse, which is the first time derivative of the power exponential pulse and is given by

$$I^T(t) = I_{\max} N \left(\frac{\nu}{t_r}\right) \left[\left(\frac{t}{t_r}\right)^{\nu-1} - \left(\frac{t}{t_r}\right)^{\nu}\right] \exp\left[-\nu\left(\frac{t}{t_r} - 1\right)\right] H(t) \tag{8.2}$$

where $I_{\max}$ represents the pulses amplitude, ν represent the rising exponent of the pulse and t_r represents the rise time, which is defined as the moment where the pulse has its first zero-crossing. The normalization constant

$$N = \frac{t_r}{\nu^{\frac{1}{2}}} \exp\left[-\nu^{\frac{1}{2}}\right] \left(\frac{\nu^{\frac{1}{2}}}{\nu^{\frac{1}{2}} - 1}\right)^{\nu-1} \tag{8.3}$$

is added to ensure a that the maximum amplitude of the pulse shape is $I_{\max}$. The pulse carries no electric charge.

Furthermore, a pulse time width t_w can be determined such that

$$t_w = t_r \nu^{-(\nu+1)} \Gamma(\nu + 1) \exp(\nu) \tag{8.4}$$

where $\Gamma(\cdot)$ represents the gamma function.

For the determination of the vector potential and the electric and magnetic field components the

first and third time derivative of the excited pulse are needed. These are given by

$$\partial_t I^T(t) = I_{\max} N \left(\frac{\nu}{t_r^2}\right) \left[(\nu-1)\left(\frac{t}{t_r}\right)^{\nu-2} - 2\nu\left(\frac{t}{t_r}\right)^{\nu-1} + \nu\left(\frac{t}{t_r}\right)^{\nu}\right] \exp\left[-\nu\left(\frac{t}{t_r}-1\right)\right] H(t) \tag{8.5}$$

$$\begin{aligned}\partial_t^3 I^T(t) = I_{\max} N \left(\frac{\nu}{t_r^4}\right) \Bigg[&(\nu-1)(\nu-2)(\nu-4)\left(\frac{t}{t_r}\right)^{\nu-4} \\ &-4\nu(\nu-1)(\nu-2)\left(\frac{t}{t_r}\right)^{\nu-3} + 3\nu^2(\nu-1)\left(\frac{t}{t_r}\right)^{\nu-2} \\ &-4\nu^3\left(\frac{t}{t_r}\right)^{\nu-1} + \nu^3\left(\frac{t}{t_r}\right)^{\nu}\Bigg] \exp\left[-\nu\left(\frac{t}{t_r}-1\right)\right] H(t)\end{aligned} \tag{8.6}$$

where it is found from (8.6) that the rising exponent of the excited pulse should be at least $\nu > 4$ in order to prevent jump discontinuities at $t = 0$ up to the third derivative. The source parameters are taken to be $A^T = 1$ m^2, $I_{\max} = 1$ mA, $t_w = 0.1$ ns and $\nu = 5$.

8.2 Validation against established results

In this section the derived method will be tested again two known results, these being (i) the electric and magnetic field components for a loop dipole antenna in free-space and (ii) the magnetic Hertzian potential for a two layer configuration with conductivity [9]. These can be combined in a single two layer configuration with a single conductive medium by taking $\varepsilon_2 = \varepsilon_1$ (Fig. 8.1). Since the direct

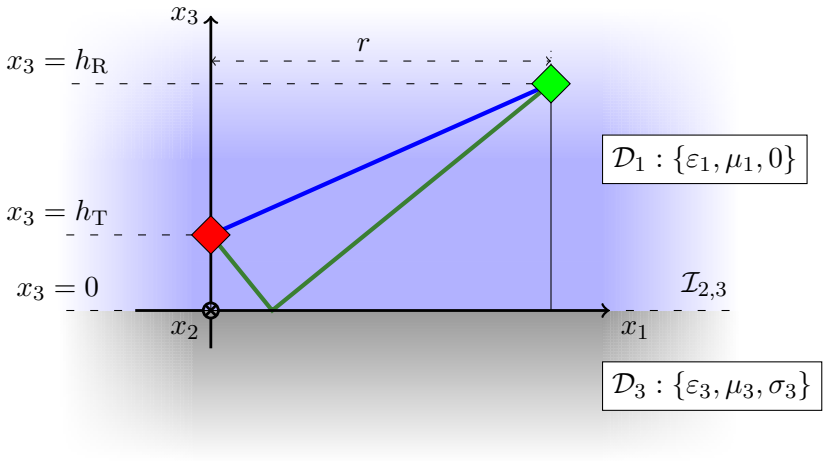

Figure 8.1: Two layer configuration that is used for testing of the numerical results. Blue corresponds to $\{j, n\} = \{0, 0\}$. Green corresponds to $\{j, n\} = \{1, 0\}$.

ray ($\{j, n\} = \{0, 0\}$) does not contain any contribution from reflection at $\mathcal{I}_{2,3}$ the resulting electric and magnetic field components at the receiver should be equal to the case of an magnetic dipole in free-space. Note that these two rays are the only ones that exist within this configuration.

The parameters used in this configuration are given in Table 8.1.

Table 8.1: Parameters of the configuration that is used for testing

Domain	Relative permittivity ε_r	Relative permeability μ_r	Conductivity σ (mSm^{-1})
$\mathcal{D}_1$	1	1	0
$\mathcal{D}_3$	10	1	$\{3, 30, 300\}$

8.2.1 A magnetic dipole in free-space

The contribution to the electric and magnetic field components that follow as a result of the direct ray ($\{j, n\} = \{0, 0\}$) can be analytically represented [5, Sec. 26.10] by

$$\boldsymbol{E} = \partial_t I(t - |\boldsymbol{X}|/c_1)\frac{\mu_1}{4\pi|\boldsymbol{X}|^2}\boldsymbol{\Theta} \times \boldsymbol{A}^T + \partial_t^2 I(t - |\boldsymbol{X}|/c_1)\frac{\mu_1}{4\pi c_1|\boldsymbol{X}|^2}\boldsymbol{\Theta} \times \boldsymbol{A}^T \tag{8.7}$$

$$\begin{aligned}\boldsymbol{H} = {} & I(t - |\boldsymbol{X}|/c_1)\frac{1}{4\pi|\boldsymbol{X}|^3}(3\boldsymbol{\Theta}\boldsymbol{\Theta}^T - \mathbb{I})\boldsymbol{A}^T + \partial_t I(t - |\boldsymbol{X}|/c_1)\frac{1}{4\pi c_1|\boldsymbol{X}|^2}(3\boldsymbol{\Theta}\boldsymbol{\Theta}^T - \mathbb{I})\boldsymbol{A}^T \\ & + \partial_t^2 I(t - |\boldsymbol{X}|/c_1)\frac{1}{4\pi c_1^2|\boldsymbol{X}|}(\boldsymbol{\Theta}\boldsymbol{\Theta}^T - \mathbb{I})\boldsymbol{A}^T\end{aligned} \tag{8.8}$$

with

$$\boldsymbol{X} = \boldsymbol{x} - \boldsymbol{x}^T \tag{8.9}$$

$$\boldsymbol{\Theta} = \frac{\boldsymbol{x} - \boldsymbol{x}^T}{|\boldsymbol{x} - \boldsymbol{x}^T|}. \tag{8.10}$$

representing the relative position and the unit vector oriented from the center of the loop to the point of observation respectively. Other parameters that are used for these numerical results are

$$r = 0.5 \cdot 10^{-3} \tag{8.11}$$

$$x_3 = 1.0 \cdot 10^{-3} \tag{8.12}$$

$$h_\mathrm{T} = 2.0 \cdot 10^{-6}. \tag{8.13}$$

The results are used to check if the symmetry is preserved after applying the method from Chapter 6. Results are shown in Fig. 8.2- 8.4 for angles $\phi = 0, 45, 90$ degrees. Where ϕ represents the angle in the cylindrical reference frame (see (1.2)-(1.4)). All magnetic field components are normalized to the maximum of the analytical solution for $\boldsymbol{H}$ (see (8.8)) . All electric field components are normalized to the maximum of the analytical solution for $\boldsymbol{E}$ (see (8.7)).

From Fig. 8.2- 8.4 it is found that there is excellent agreement between the numerical results (in blue) and the analytic results from (8.7)-(8.8) (in green). It must be noted that the numerical solutions deviates from the analytical solutions on two points.

First, the late time signature (i.e. for $t \gg T(0)$), the numerical result deviates away from zero due to the fact the source signature never vanishes. This has the consequence that in the convolution a cumulative error is introduced. However, the effect of this error can easily be manipulated by proper choice of the sample time, as well choosing a relevant observation time window.

Secondly, where the electric and magnetic field components are to be zero as a result of the symmetry conditions (E_1 and H_2 when $\phi = 0, \pi$ and H_1 and E_2 when $\phi = -\frac{\pi}{2}, \frac{\pi}{2}$) some numerical noise is found to be present. However, the magnitude is very small compared to the magnitude of the other components (roughly an order 10^{20} smaller).

8.2.2 Reflection with a conducting layer

The magnetic Hertzian potential that follows as a result a ray which has undergone a single reflection at $\mathcal{I}_{2,3}$ ($\{j,n\} = \{1,0\}$) has been derived in [9]. This test allows for verification of the method derived for determining the magnetic Hertzian potential.

Since in [9] the source has already been defined, a different source from the monocycle pulse in Section 8.1 has been used. The source signature of the magnetic moment has been taken to be a rectangular pulse

$$f(t) = \frac{1}{T_{\text{pulse}}}\left[H(t) - H(t - T_{\text{pulse}})\right] \tag{8.14}$$

with $T_{\text{pulse}} = 1$ ms. The first time derivative of the source signature then yields

$$f(t) = \frac{1}{T_{\text{pulse}}}\left[\delta(t) - \delta(t - T_{\text{pulse}})\right] \tag{8.15}$$

which represents the scaled Green's function (by T_{pulse}^{-1}), subtracted by a delayed version of itself.

Original results where replicated using the derived expression in [9]. These are given by

$$u^{\text{T};2,1} = \int_{\tau=T(0)}^{t} \partial_t f(t-\tau)\left[g_1 + g_2 + g_3 + g_4\right] \mathrm{d}\tau \tag{8.16}$$

with

$$g_1 = \frac{H(t-T(0)}{2\pi^2}\int_0^{Q(\tau)} \frac{\mathrm{Re}\left\{\frac{\bar{\gamma}_1 - \bar{\gamma}_3}{\bar{\gamma}_1 + \bar{\gamma}_3}\right\}}{\left[\tau^2 - T^2(q)\right]^{\frac{1}{2}}}\mathrm{d}q \tag{8.17}$$

$$g_2 = \frac{H(t-T(0)}{2\pi^2}\int_0^{Q(\tau)} \frac{\mathrm{Re}\left\{\frac{2\bar{\gamma}_1}{\bar{\gamma}_3} - \frac{\bar{\gamma}_1 - \bar{\gamma}_3}{\bar{\gamma}_1 + \bar{\gamma}_3} - 1\right\}}{\left[\tau^2 - T^2(q)\right]^{\frac{1}{2}}}\mathrm{d}q * \Delta\exp[-\Delta\tau]H(t) \tag{8.18}$$

$$g_3 = \frac{H(t-T(0)}{2\pi^2}\int_0^{Q(\tau)}\int_{\xi=T(q)}^{\tau} \frac{\mathrm{Re}\left\{-\Delta\frac{\bar{\gamma}_1}{\bar{\gamma}_3}\left[I_0(\frac{\sigma_3\mu_3(\tau-\xi)}{2\bar{\gamma}_3^2}) - I_1(\frac{\sigma_3\mu_3(\tau-\xi)}{2\bar{\gamma}_3^2})\right]\exp\left[-\frac{\sigma_3\mu_3(\tau-\xi)}{2\bar{\gamma}_3^2}\right]\right\}}{\left[\xi^2 - T^2(q)\right]^{\frac{1}{2}}}\mathrm{d}\xi\mathrm{d}q \tag{8.19}$$

$$g_4 = \frac{H(t-T(0)}{2\pi^2}\int_0^{Q(\tau)}\int_{\xi=T(q)}^{\tau} \frac{\mathrm{Re}\left\{\Delta\left(\frac{\bar{\gamma}_1}{\bar{\gamma}_3}\right)^3\left[I_0(\frac{\sigma_3\mu_3(\tau-\xi)}{2\bar{\gamma}_3^2}) - I_1(\frac{\sigma_3\mu_3(\tau-\xi)}{2\bar{\gamma}_3^2})\right]\exp\left[-\frac{\sigma_3\mu_3(\tau-\xi)}{2\bar{\gamma}_3^2}\right]\right\}}{\left[\xi^2 - T^2(q)\right]^{\frac{1}{2}}}\mathrm{d}\xi\mathrm{d}q$$
$$*\Delta\exp[-\Delta\tau]H(t) \tag{8.20}$$

where $\Delta = \sigma_3(\varepsilon_3 - \varepsilon_1)^{-1}$. The star symbol $*$ denotes convolution with respect to τ. Furthermore, in [9] the assumption is made that the contribution of $\Delta\exp[-\Delta\tau]$ can be approximated by a Dirac delta function due to the high value of Δ and the large decay for each numerically discretized time step.

Figures 8.5a and 8.5b show replicated results, whereas Figures 8.5c and 8.5d show numerical results generated by the method derived in this thesis. It is noted that the results in Fig. 8.5c start to deviate from the results in Fig. 8.5a for lower values of σ_3. This could possibly explained by the previously mentioned approximation that $\Delta\exp[-\Delta\tau] \approx \delta(\tau)$, which is not included in the method derived in this thesis.

8.3 Investigation of a realistic configuration

In this section results are presented that show the behavior of the electric and magnetic field components outside the IC when the transmit antenna is excited using the pulse described Section 8.1. The values for the permittivity ε_r and the permeability μ_r are given in Table 2.1. Furthermore, the antenna height is taken to be $h_{\mathrm{T}} = 2 \cdot 10^{-6}$ and the height of $\mathcal{I}_{2,1}$ is taken to be $d = 7 \cdot 10^{-6}$. The numerical experiments can be divided in two sets, in which (i) the observation distance and (ii) the conductivity σ_3 was varied (see Table 8.2). For all experiments the angle ϕ is taken to be zero, thereby reducing the result to the three non-zero components H_1, E_2 and H_3. For every experiment all rays up to three reflections with $\mathcal{I}_{2,1}$ ($n = 3$) have been determined, resulting in a total of eight rays. Furthermore, the sum of these eight rays are compared with the analytical result in free space (see (8.7)-(8.8)) in order to give an indication of the deviation due to the multilayer structure. All magnetic field components are normalized to the maximum of the analytical solution for $\boldsymbol{H}$ (see (8.8)) . All electric field components are normalized to the maximum of the analytical solution for $\boldsymbol{E}$ (see (8.7)).

Table 8.2: Parameters of the configuration that is used for testing

	Experiment 1 (Fig. 8.6)	Experiment 2 (Fig. 8.7)	Experiment 3 (Fig. 8.8)	Experiment 4 (Fig. 8.9)	Experiment 5 (Fig. 8.10)
r (m)	$0.5 \cdot 10{-}4$	$0.5 \cdot 10^{-2}$	$0.5 \cdot 10^{-1}$	$0.5 \cdot 10^{-2}$	$0.5 \cdot 10^{-2}$
x_3 (m)	$1 \cdot 10^{-3}$	$1 \cdot 10^{-2}$	$1 \cdot 10^{-1}$	$1 \cdot 10^{-2}$	$1 \cdot 10^{-2}$
σ_3 (mSm^{-1})	1	1	1	0	∞

One of the observation that can be made upon inspection of these first results is that when the point of observation is very close to the antenna in experiment 1 (Fig. 8.6) there is almost no contribution from any ray other that the direct ray ($[j, n] = [0, 0]$). However, when increasing the distance in experiments 2 and 3 (Fig. 8.7-8.8) the contributions of the other rays become more significant and result an attenuation of the field at the point of observation with respect to the analytical free-space result.

For experiments 4 and 5 (Fig. 8.9-8.10) the distance values of experiment 2 have been used, but in these experiments the medium in $\mathcal{D}_3$ is lossless ($\sigma_3 = 0$) and perfectly conducting ($\sigma = \infty$) respectively. When comparing the results of experiments 4 and 5 with the results from experiment 2 it can be seen that the realistic model, with a value of $\sigma_3 = 1 \cdot 10^{-1}$ corresponding to silicon, is almost equal to the lossless model.

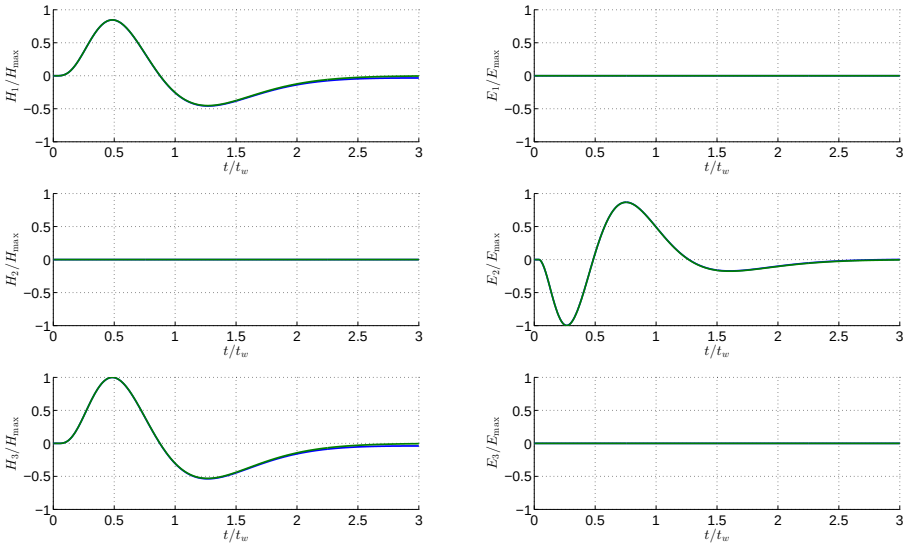

Figure 8.2: Numerical results (blue) and analytical results (green) for a magnetic dipole in free-space. $\phi = 0$ degrees

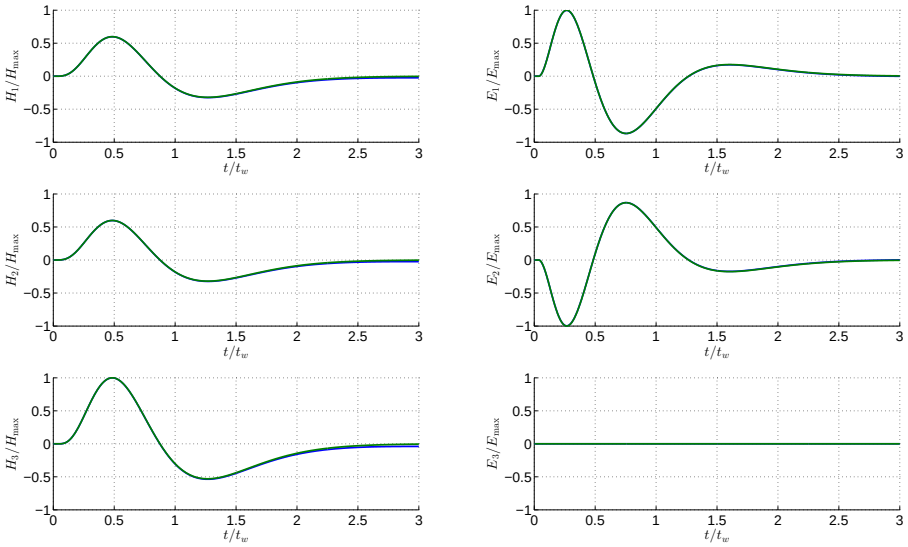

Figure 8.3: Numerical results (blue) and analytical results (green) for a magnetic dipole in free-space. $\phi = 45$ degrees

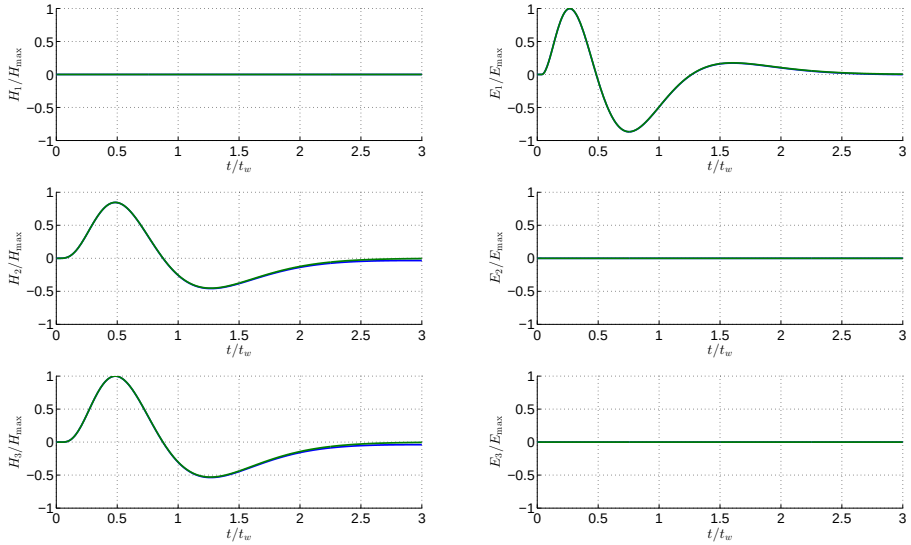

Figure 8.4: Numerical results (blue) and analytical results (green) for a magnetic dipole in free-space. $\phi = 90$ degrees

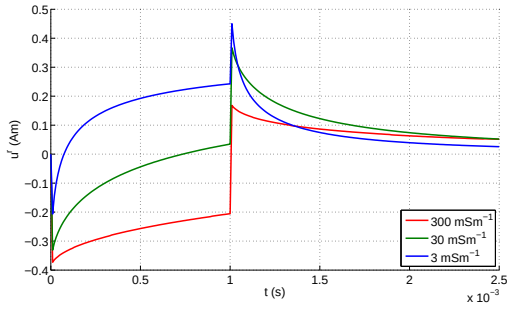

(a) Original results on a time interval of 2.5 times the pulse width. [Replicated based on [9] with the permission of the author]

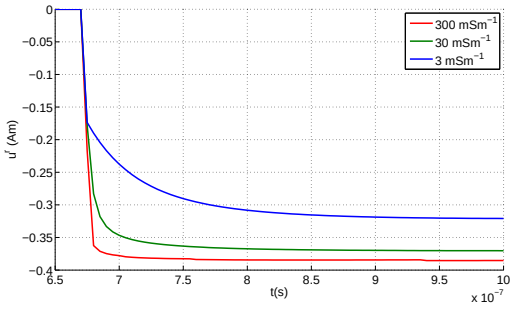

(b) Original results zoomed in around the arrival time $T(0)$. [Replicated based on [9] with the permission of the author]

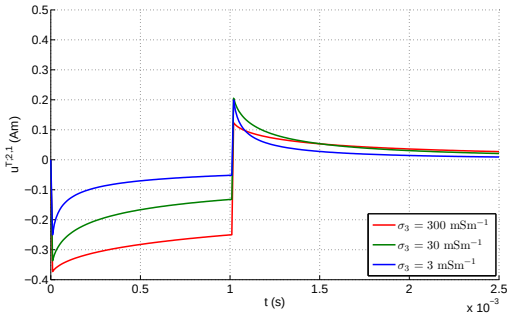

(c) On a time interval of 2.5 times the pulse width

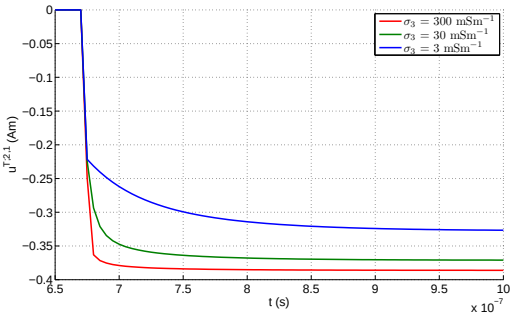

(d) Zoomed in around the arrival time $T(0)$.

Figure 8.5: Magnetic Hertzian potential of a reflected ray $\{j, n\} = \{1, 0\}$.

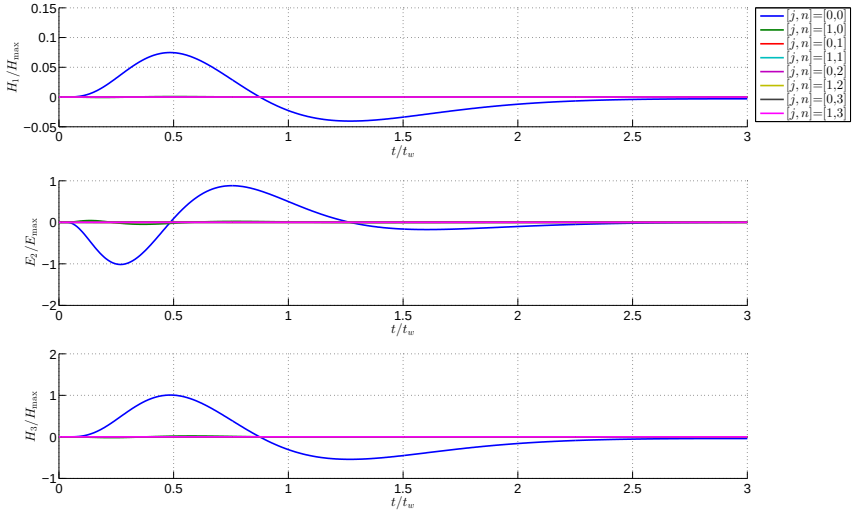

(a) Ray contributions in the field components H_1, E_2 and H_3

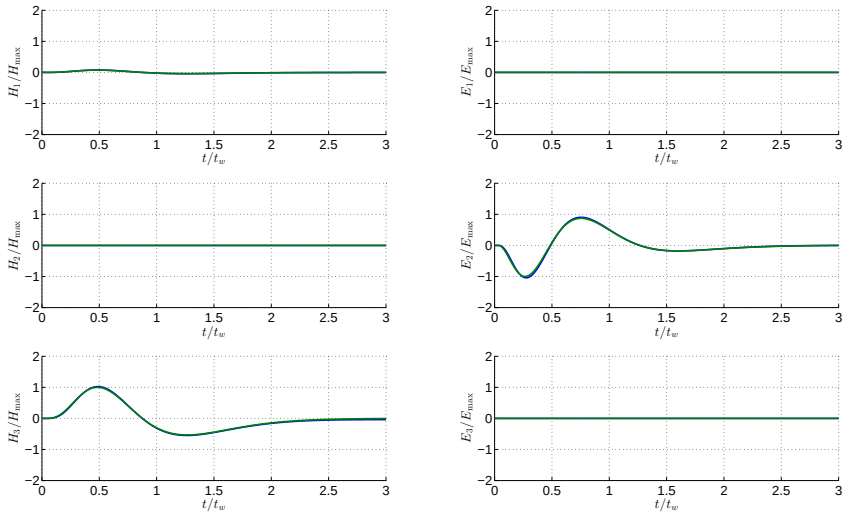

(b) Sum of the ray contribution in 8.6a (in blue) compared with the analytical result for free-space (in green)

Figure 8.6: Experiment 1 ($r = 0.5 \cdot 10^{-4}$ m, $x_3 = 1 \cdot 10^{-3}$ m and $\sigma_3 = 1$ mSm^{-1})

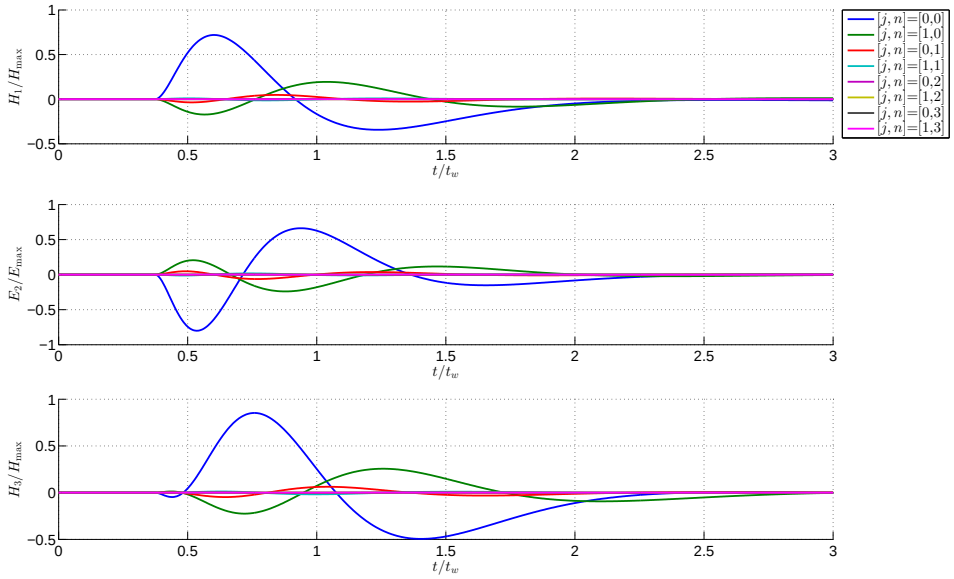

(a) Ray contributions in the field components H_1, E_2 and H_3

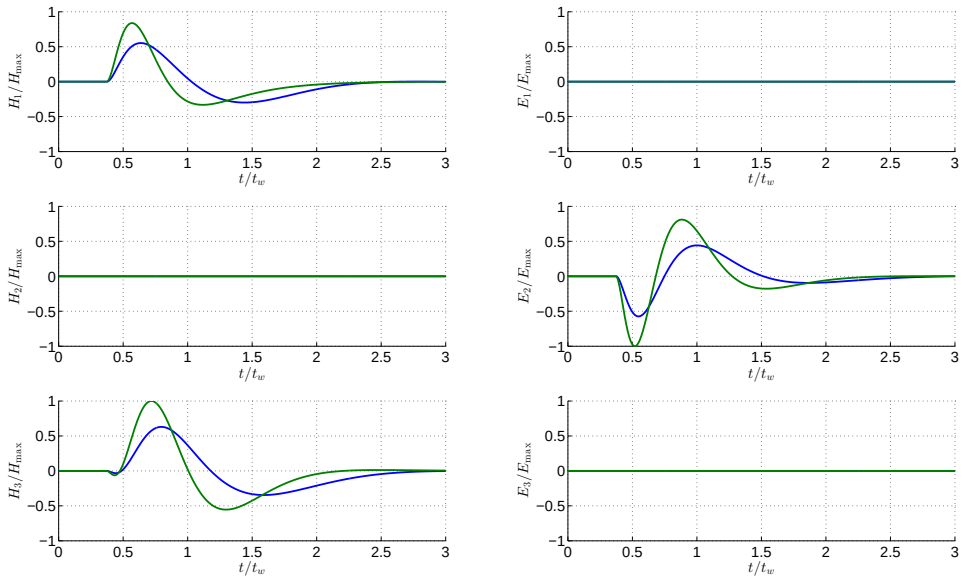

(b) Sum of the ray contribution in 8.7a (in blue) compared with the analytical result for free-space (in green)

Figure 8.7: Experiment 2 ($r = 0.5 \cdot 10^{-2}$ m, $x_3 = 1 \cdot 10^{-2}$ m and $\sigma_3 = 1$ mSm^{-1})

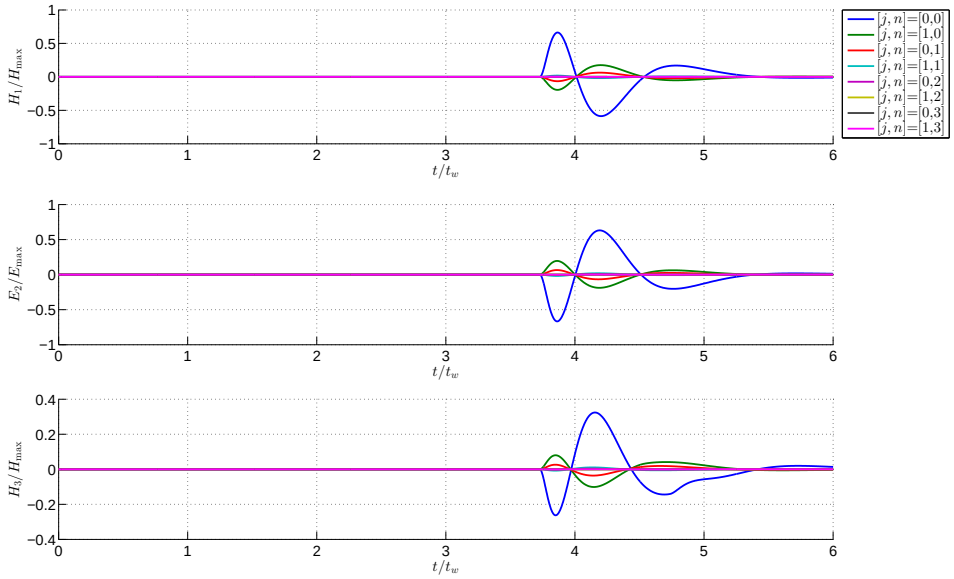

(a) Ray contributions in the field components H_1, E_2 and H_3

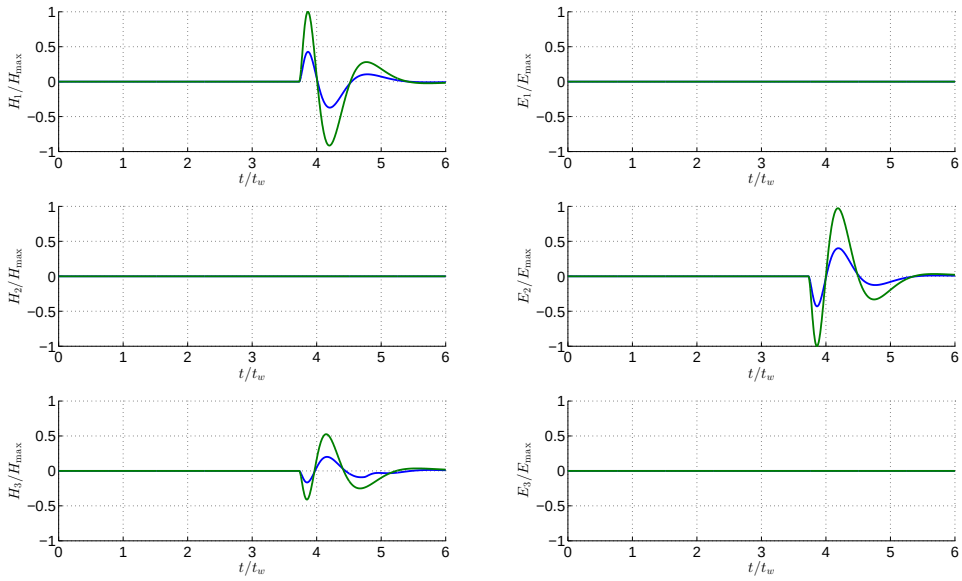

(b) Sum of the ray contribution in 8.8a (in blue) compared with the analytical result for free-space (in green)

Figure 8.8: Experiment 3 ($r = 0.5 \cdot 10^{-1}$ m, $x_3 = 1 \cdot 10^{-1}$ m and $\sigma_3 = 1$ mSm^{-1})

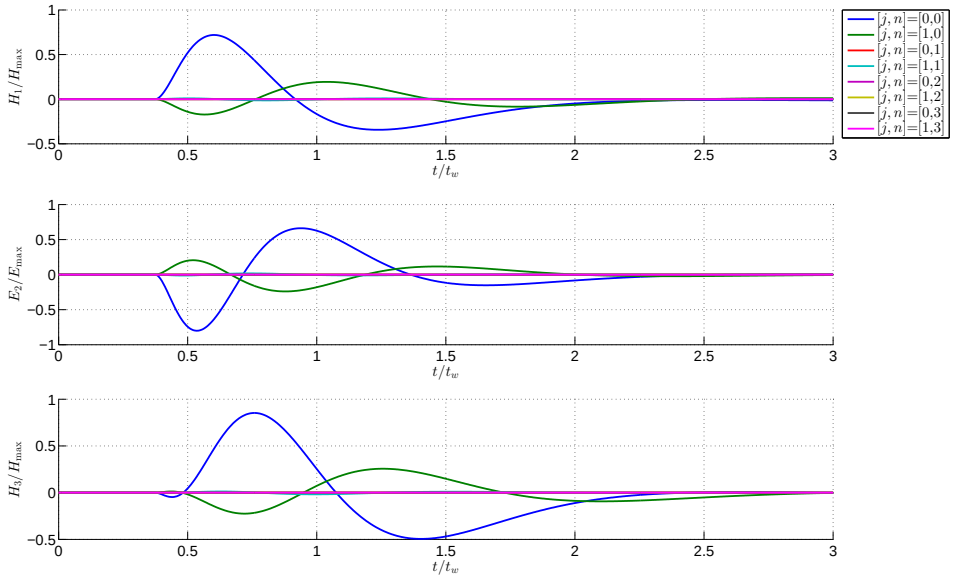

(a) Ray contributions in the field components H_1, E_2 and H_3

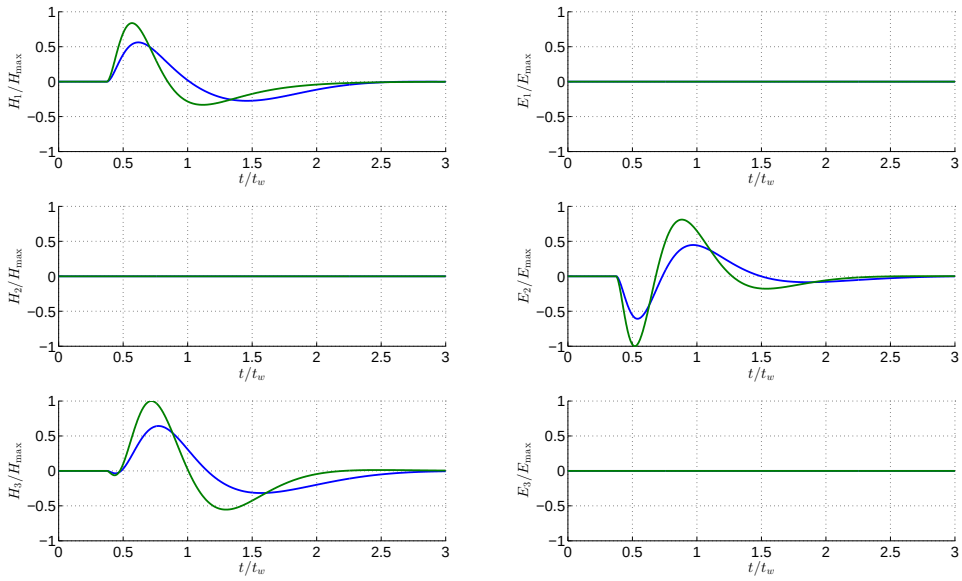

(b) Sum of the ray contribution in 8.9a (in blue) compared with the analytical result for free-space (in green)

Figure 8.9: Experiment 4 ($r = 0.5 \cdot 10^{-2}$ m, $x_3 = 1 \cdot 10^{-2}$ m and $\sigma_3 = 0$ mSm^{-1})

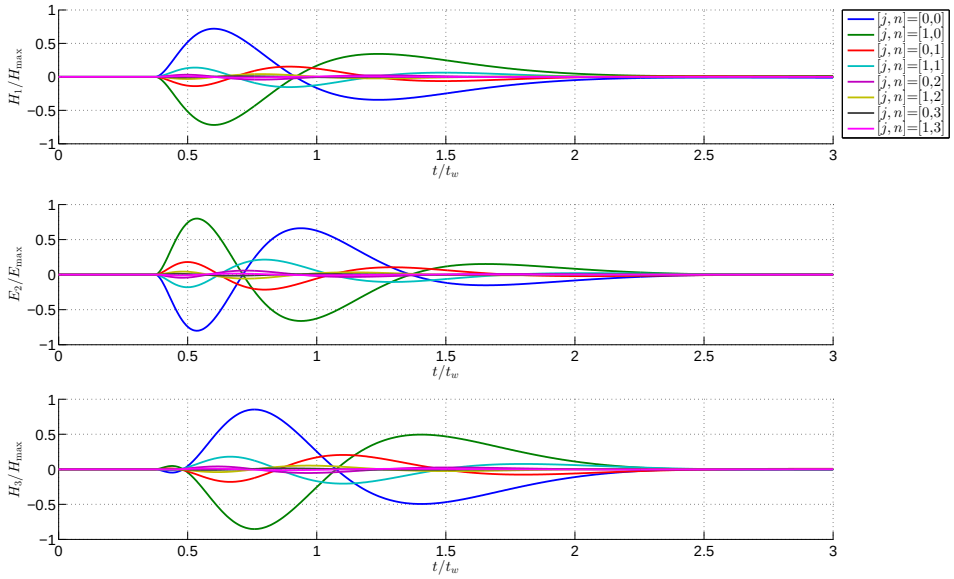

(a) Ray contributions in the field components H_1, E_2 and H_3

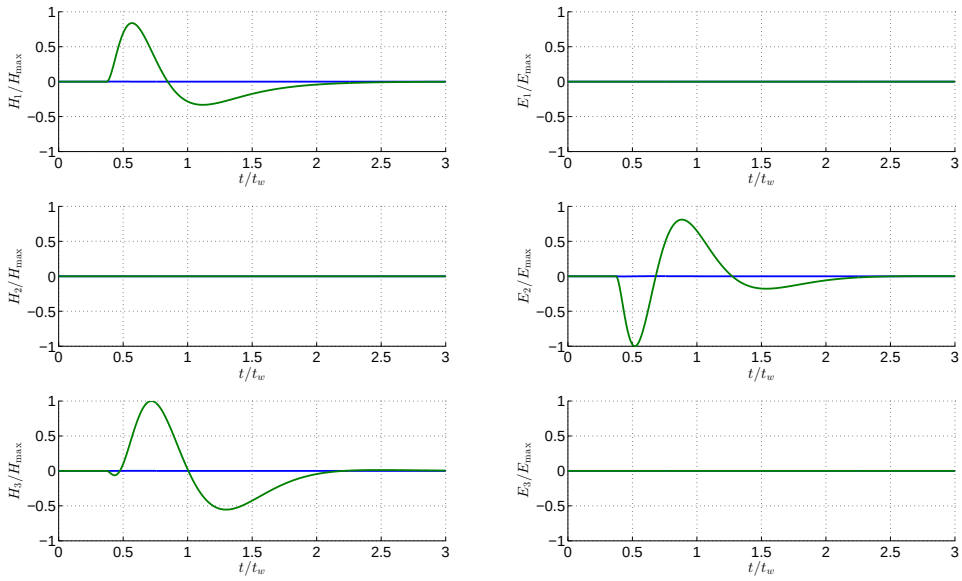

(b) Sum of the ray contribution in 8.10a (in blue) compared with the analytical result for free-space (in green)

Figure 8.10: Experiment 5 ($r = 0.5 \cdot 10^{-2}$ m, $x_3 = 1 \cdot 10^{-2}$ m and $\sigma_3 = \infty$ mSm^{-1})

Chapter 9

Conclusion and future work

In this thesis a model has been derived which allows the determination of closed-form time-domain solutions of the electric and magnetic field components outside an IC. A multi-layered configuration which is representative for an integrated loop antenna provided the basis which allowed for employing the Cagniard-DeHoop method. Due to the highly conductive substrate, losses due to conductivity have also been taken into account.

The transmit antenna has been taken to be an electrically small loop antenna, that was modeled as a vertical magnetic dipole. This allowed for a full characterization of the electric and magnetic field components in three dimensions by a single magnetic Hertzian potential function.

In order to retrieve the electric and magnetic field components from this potential function, several differentiations with respect to both spatial and time coordinates have to be applied. A method to include these differentiations by applying them before transforming the function back to space and time domain has been presented.

The accuracy of the proposed method was assessed by examining a two layer test configuration. This study focused on two aspects: (i) identification of the symmetry in the problem and (ii) verifying the interaction of the potential with the conductive medium by using known results.

The first test showed excellent agreement between the analytical and numerical result from the method, whereas the first test showed a deviation in the potential function for smaller values of σ. The latter can possibly explained via an assumption made in [9].

Observations based on the first numerical experiments with the examined configuration (with realistic parameter values) have shown that for very small distances from the transmit antenna the electric and magnetic field components are almost the same as their equivalents in free-space configurations. For greater distances the contribution of reflections become more significant. Furthermore, a second observation, which followed from a comparison between the realistic model and two models where $\mathcal{D}_3$ are non-conducting and perfectly conducting, has shown that the non-conducting model gives an almost equal numerical result as the realistic model.

This work can be seen as a first step towards deriving an analytical model which can provide indications and insight into the various mechanisms that occur during inter-chip communication. This thesis has been focused on the field outside an IC, therefore the logical next step would be to extend this work to determine the field intercepted by an antenna located in a neighboring IC. Furthermore, future work should focus on deriving functions for the generated voltage in a receive antenna by the general Lorentz electromagnetic reciprocity theorem.

The main focus however, should lie on conducting many more experiments with the model which was examined in this thesis. Following the first observations, this could lead to a set of approximations which would allow for the determination of the above mentioned field and voltage using available

knowledge. Two examples will be mentioned here: if (i) this model can show that for points of observations very close to the antenna the field can be approximated by a free-space model one could use the previous work [10] for a first approximation; (ii) if from further experiments it is found that the conductivity of the silicon can be neglected in a first approximation, this would imply that the field which would be intercepted by an antenna in a neighboring IC can be determined using a generalized ray theory model for a lossless horizontally layered medium can be used [19].

Appendix A

Pole contribution at τ

In Chapter 6 an operation of a single or double integration and differentiation with respect to s is performed. This is necessary to ensure that the conditions for the application of Jordan's lemma are met. However, this is at the cost of introducing a possible first or second order pole in $\tau = \omega r + \bar{\gamma}_1 Z_1 + \bar{\gamma}_2 Z_{2,j}(n) + \kappa = 0$. This appendix will the determine the contribution of the residues that follow from this pole contributions.

When reducing the examined configuration to a two layer configuration such that $\bar{\gamma}_1 = \bar{\gamma}_2$ (see Fig. 8.1) one obtains an analytical representation for the pole given by

$$\omega_p = \frac{\Omega(Z_1 + Z_2(n))}{R} \tag{A.1}$$

where ω_p denotes the value of ω such that $\tau(\omega_p) = 0$. In (A.1) $\Omega = \Omega_1 = \Omega_2$. The point of intersection of the contour $\mathcal{C} \cup \mathcal{C}^*$ with the real ω-axis is given by

$$\omega_0 = \frac{\Omega r}{R} \tag{A.2}$$

which shows that the pole can very well lie within the closed contour ($\{A, E, D, C, B\}$ in 5.1 for $Z < r$.

A.1 First order pole

This section will discuss the contribution that is introduced in the electric field components as a result of the first order pole. First, (6.18) is rewritten as

$$\hat{m}_{j,n}(\boldsymbol{x}, s, p) = \frac{\mathrm{d}}{\mathrm{d}s}\left[\frac{1}{8\pi^2}\int_{q=-\infty}^{\infty}\int_{\omega(\tau)=-\mathrm{i}\infty}^{\mathrm{i}\infty}\int_{\kappa=0}^{\infty}\frac{\hat{W}^E_{j,n}(\omega(\tau), q, p)}{\tau}\mathrm{d}\kappa\mathrm{d}\omega(\tau)\mathrm{d}q\right] \tag{A.3}$$

where the parameterization (5.22) has been applied. The function $\hat{W}^E_{j,n}$ is given by

$$\hat{W}^E_{j,n}(\omega, q, p) = \mathrm{i}\hat{M}^E_{j,n}(\omega(\tau), q, p)\exp\left[-s\tau\right]. \tag{A.4}$$

By introducing the variable ω_p as the value for which $\tau = 0$ it is possible to determine the residue as

$$\begin{aligned}\mathrm{Res}(\hat{W}^E_{j,n}(\omega, q, p), \omega_p) &= \lim_{\omega(\tau)\to\omega_p}\hat{W}^E_{j,n}(\omega, q, p) \\ &= \hat{W}^E_{j,n}(\omega_p, q, p) = \mathrm{i}\hat{M}^E_{j,n}(\omega_p, q, p)\end{aligned} \tag{A.5}$$

where the exponent term has vanished from $\hat{W}^E_{j,n}(\omega_p, q, p)$ since the function in its argument is τ and, therefore, the argument of the exponent is zero. Furthermore, by inspection of (6.16) it is found that $\hat{M}^E_{j,n}(\omega_p, q, p)$ exists and is finite for $\omega = \omega_p$ since the $\bar{\gamma}_2$ term in its denominator is only zero for $\omega = \Omega_2$. Since by virtue of Snell's law (see (5.26)) it is guaranteed that the contour $\mathcal{C} \cup \mathcal{C}^*$ intersects the real ω-axis between in $\omega_0 < \Omega_{\min}$ the pole would then lie outside the closed contour and would therefore not be of relevance for the contour deformation.

Using (A.5) the integral with respect to ω in (A.3) can now be deformed, which yields

$$\begin{aligned}\hat{m}^E_{j,n}(\boldsymbol{x}, s, p) = \frac{\mathrm{d}}{\mathrm{d}s}\left[\frac{-1}{4\pi^2}\int_{q=-\infty}^{\infty}\int_{\xi=T(q)}^{\infty}\int_{\tau=\xi}^{\infty}\mathrm{Im}\left\{\frac{\hat{M}^E_{j,n}(\omega(\tau), q, p)\exp[-s\tau]}{(r-\omega Z_1\bar{\gamma}_1^{-1}-\omega Z_{2,j}(n))\tau}\right\}\mathrm{d}\tau\mathrm{d}\xi\mathrm{d}q\right] \\ -\frac{\mathrm{d}}{\mathrm{d}s}\int_{q=-\infty}^{\infty}\left[2\pi\hat{M}^E_{j,n}(\omega_p, q, p)\mathrm{d}q\right]\end{aligned} \tag{A.6}$$

where the second term on the right hand side vanishes since $\hat{M}^E_{j,n}(\omega_p, q, p)$ has no dependence on s. As a result, (A.6) reduces to

$$\hat{m}^E_{j,n}(\boldsymbol{x}, s, p) = \frac{\mathrm{d}}{\mathrm{d}s}\left[\frac{-1}{4\pi^2}\int_{q=-\infty}^{\infty}\int_{\xi=T(q)}^{\infty}\int_{\tau=\xi}^{\infty}\mathrm{Im}\left\{\frac{\hat{M}^E_{j,n}(\omega, q, p)\exp[-s\tau]}{(r-\omega Z_1\bar{\gamma}_1^{-1}-\omega Z_{2,j}(n))\tau}\right\}\mathrm{d}\tau\mathrm{d}\xi\mathrm{d}q\right]. \tag{A.7}$$

A.2 Second order pole

This section will discuss the contribution that is introduced in the electric field components as a result of the first order pole. First, (6.28) is rewritten as

$$\hat{m}^H_{j,n}(\boldsymbol{x}, s, p) = \frac{\mathrm{d}^2}{\mathrm{d}s^2}\left[\frac{-1}{8\pi^2}\int_{q=-\infty}^{\infty}\int_{\omega(\tau)=-\mathrm{i}\infty}^{\mathrm{i}\infty}\int_{\kappa=0}^{\infty}\frac{\hat{W}^H_{j,n}(\omega(\tau), q, p)}{\tau^2}\mathrm{d}\kappa\mathrm{d}\omega(\tau)\mathrm{d}q\right] \tag{A.8}$$

where the parameterization (5.22) has been applied. The function $\hat{W}^H_{j,n}$ is given by

$$\hat{W}^H_{j,n}(\omega, q, p) = \mathrm{i}\hat{M}^H_{j,n}(\omega(\tau), q, p)\exp\left[-s\tau\right]. \tag{A.9}$$

The residue for the second order pole in $\omega = \omega_p$ is then given by

$$\begin{aligned}\mathrm{Res}(\hat{W}^H_{j,n}(\omega(\tau), q, p), \omega_p) &= \lim_{\omega(\tau)\to\omega_p}\frac{\mathrm{d}}{\mathrm{d}\omega(\tau)}\left[\hat{W}^H_{j,n}(\omega(\tau), q, p)\right] \\ &= \lim_{\omega(\tau)\to\omega_p}\Big[-s\left[r-\omega(\tau)\bar{\gamma}_1^{-1}(Z_1-\omega(\tau)\bar{\gamma}_2^{-1}Z_{2,j}(n)\right]\mathrm{i}\hat{M}^H_{j,n}(\omega(\tau), q, p) \\ &\quad \exp[-s\tau] + \frac{\mathrm{d}}{\mathrm{d}\omega(\tau)}\left\{\mathrm{i}\hat{M}^H_{j,n}(\omega(\tau), q, p)\right\}\exp[-s\tau]\Big] \\ &= -s\left[r-\omega_p\bar{\gamma}_1^{-1}Z_1-\omega_p\bar{\gamma}_2^{-1}Z_{2,j}(n)\right]\mathrm{i}\hat{M}^H_{j,n}(\omega_p, q, p) \\ &\quad + \frac{\mathrm{d}}{\mathrm{d}\omega(\tau)}\left\{\mathrm{i}\hat{M}^H_{j,n}(\omega(\tau), q, p)\right\}\Big|_{\omega(\tau)=\omega_p} \\ &= a(\omega_p, q, p)s + b(\omega_p, q, p)\end{aligned} \tag{A.10}$$

where

$$a(\omega_p, q, p) = -\mathrm{i}\left[r-\omega_p\bar{\gamma}_1^{-1}Z_1-\omega_p\bar{\gamma}_2^{-1}Z_{2,j}(n)\right]\hat{M}^H_{j,n}(\omega_p, q, p) \tag{A.11}$$

$$b(\omega_p, q, p) = \frac{\mathrm{d}}{\mathrm{d}\omega(\tau)}\left\{\mathrm{i}\hat{M}^H_{j,n}(\omega(\tau), q, p)\right\}\Big|_{\omega(\tau)=\omega_p}. \tag{A.12}$$

Note that both (A.11) and (A.12) exist and are finite since again there is only division by the propagation factors $\bar{\gamma}_i$ $(i = 1, 2, 3)$, which can only be zero when the pole lies outside the closed contour, as was discussed in Section A.1. Using (A.10) the integral with respect to ω can now be deformed, which yields

$$\hat{m}^H_{j,n}(\boldsymbol{x}, s, p) = \frac{\mathrm{d}^2}{\mathrm{d}s^2}\left[\frac{1}{4\pi^2}\int_{q=-\infty}^{\infty}\int_{\xi=T(q)}^{\infty}\int_{\tau=\xi}^{\infty}\mathrm{Im}\left\{\frac{\hat{M}^H_{j,n}(\omega, q, p)\exp[-s\tau]}{(r - \omega Z_1\bar{\gamma}_1^{-1} - \omega Z_{2,j}(n))\tau^2}\right\}\mathrm{d}\tau\mathrm{d}\xi\mathrm{d}q\right]$$
$$-\frac{\mathrm{d}^2}{\mathrm{d}s^2}\int_{q=-\infty}^{\infty}\left[2\pi\left[a(\omega_p, q, p)s + b(\omega_p, q, p)\right]\mathrm{d}q\right] \tag{A.13}$$

where the second term on the right hand side vanishes since a second order differentiation of a first order polynomial is equal to zero. As a result, (A.13) reduces to

$$\hat{m}^H_{j,n}(\boldsymbol{x}, s, p) = \frac{\mathrm{d}^2}{\mathrm{d}s^2}\left[\frac{1}{4\pi^2}\int_{q=-\infty}^{\infty}\int_{\xi=T(q)}^{\infty}\int_{\tau=\xi}^{\infty}\mathrm{Im}\left\{\frac{\hat{M}^H_{j,n}(\omega, q, p)\exp[-s\tau]}{(r - \omega Z_1\bar{\gamma}_1^{-1} - \omega Z_{2,j}(n))\tau^2}\right\}\mathrm{d}\tau\mathrm{d}\xi\mathrm{d}q\right]. \tag{A.14}$$

Bibliography

[1] M.T. Bohr and Y. A. El-Mansy. Technology for advanced high-performance microprocessors. *Electron Devices, IEEE Transactions on*, 45(3):620–625, 1998.

[2] M.-C.F. Chang, V.P. Roychowdhury, Liyang Zhang, Hyunchol Shin, and Yongxi Qian. Rf/wireless interconnect for inter- and intra-chip communications. *Proceedings of the IEEE*, 89(4):456–466, 2001.

[3] J.A. Davis, R. Venkatesan, A. Kaloyeros, M. Beylansky, S.J. Souri, K. Banerjee, K.C. Saraswat, A. Rahman, R. Reif, and J.D. Meindl. Interconnect limits on gigascale integration (gsi) in the 21st century. *Proceedings of the IEEE*, 89(3):305–324, 2001.

[4] A.T. de Hoop. Pulsed electromagnetic radiation from a line source in a two-media configuration. *Radio Science*, 14(2):253–268, 1979.

[5] A.T. de Hoop. *Handbook of Radiation and Scattering of Waves*. Academic Press, 1995.

[6] A.T. de Hoop. Transient diffusive electromagnetic fields in stratified media: Calculation of the two-dimensional e-polarized field. *Radio Science*, 35(2):443–453, 2000.

[7] A.T. de Hoop and H.J. Frankena. Radiation of pulses generated by a vertical electric dipole above a plane, non-conducting, earth. *Applied Scientific Research, Section B*, 8(1):369–377, 1960.

[8] B.A. Floyd, Chih-Ming Hung, and K.K. O. Intra-chip wireless interconnect for clock distribution implemented with integrated antennas, receivers, and transmitters. *Solid-State Circuits, IEEE Journal of*, 37(5):543–552, 2002.

[9] B.J. Kooij. Transient electromagnetic field of a vertical magnetic dipole above a plane conducting earth. *Radio Science*, 25(4):349–356, 1990.

[10] I.E. Lager and A.T. De Hoop. Loop-to-loop pulsed electromagnetic field wireless signal transfer. In *Proceedings of the 6th European Conference on Antennas and Propagation – EuCAP*, pages 786–790. IEEE, 2012.

[11] J.D. Meindl. Interconnect opportunities for gigascale integration. *Micro, IEEE*, 23(3):28–35, 2003.

[12] E. Mollick. Establishing moore's law. *Annals of the History of Computing, IEEE*, 28(3):62–75, 2006.

[13] G.E. Moore. Cramming more components onto integrated circuits. *Electronics*, 38(8):114 ff., 1965.

[14] G.E. Moore. Excerpts from a conversation with gordon moore: Moores law. *Video Transcript, Intel*, 2005.

[15] K.K. O, Kihong Kim, B.A. Floyd, J.L. Mehta, Hyun Yoon, Chih-Ming Hung, D. Bravo, T.O. Dickson, Xiaoling Guo, Ran Li, N. Trichy, J. Caserta, II Bomstad, W.R., J. Branch, Dong-Jun Yang, J. Bohorquez, Eunyoung Seok, Li Gao, A. Sugavanam, J. J Lin, Jie Chen, and J.E. Brewer. On-chip antennas in silicon ics and their application. *Electron Devices, IEEE Transactions on*, 52(7):1312–1323, 2005.

[16] Pran Kanai Saha, Nobuo Sasaki, and Takamaro Kikkawa. A cmos monocycle pulse generation circuit in a ultra-wideband transmitter for intra/inter chip wireless interconnection. *Japanese Journal of Applied Physics*, 44(4B):2104–2108, 2005.

[17] K.C. Saraswat and F. Mohammadi. Effect of scaling of interconnections on the time delay of vlsi circuits. *Solid-State Circuits, IEEE Journal of*, 17(2):275–280, 1982.

[18] J.A. Stratton. *Electromagnetic Theory*. McGraw-Hill, New York, 1941.

[19] M. Stumpf, A.T. de Hoop, and A.E. Vandenbosch. Generalized ray theory for time-domain electromagnetic fields in horizontally layered media. *IEEE Transactions on antennas and propagation*, 61(5), 2013.

[20] M.D. Verweij. *Transient acoustic waves in continuously layered media*. Delft University Press, 1992.

[21] V. Voogt, I.E. Lager, and B.J. Kooij. Loop-to-loop pulsed electromagnetic field signal transfer in layered configurations - application to inter-chip wireless communication. In *Proceedings of the 7th European Conference on Antennas and Propagation – EuCAP*, pages 952–956, 2013.

[22] M. Štumpf. *Pulsed electromagnetic field radiation from slot antennas*. PhD thesis, Brno University of Technology, 2011.

[23] M. Štumpf and A.E. Vandenbosch. On the limitations of the time-domain impedance boundary condition: line-source excited response of a conducting half-space. *[In Press]*, 2012.

[24] D.V. Widder. *The Laplace Transform*. Princeton University Press, 1946.

[25] Yuanjin Zheng, Yueping Zhang, and Yan Tong. A novel wireless interconnect technology using impulse radio for interchip communications. *Microwave Theory and Techniques, IEEE Transactions on*, 54(4):1912–1920, 2006.